

LÍVIA BUENO REIS

Parametric geometry optimization of an ejector for compression

São Paulo
2021

LÍVIA BUENO REIS

Parametric geometry optimization of an ejector for compression

Corrected version

Master thesis submitted to the Department of Mining and Petroleum Engineering (PMI), Escola Politécnica of Universidade de São Paulo (EP/USP) to obtain the title of Master of Science.

São Paulo
2021

LÍVIA BUENO REIS

Parametric geometry optimization of an ejector for compression

Corrected version

Master thesis submitted to the Department of Mining and Petroleum Engineering (PMI), Escola Politécnica of Universidade de São Paulo (EP/USP) to obtain the title of Master of Science.

Concentration area: Mineral Engineering

Advisor: Prof. Dr. Rafael dos Santos Gioria

São Paulo
2021

Autorizo a reprodução e divulgação total ou parcial deste trabalho, por qualquer meio convencional ou eletrônico, para fins de estudo e pesquisa, desde que citada a fonte.

Este exemplar foi revisado e corrigido em relação à versão original, sob responsabilidade única do autor e com a anuência de seu orientador.

São Paulo, 14 de maio de 2021

Assinatura do autor: Livia Bueno Reis

Assinatura do orientador: Rafael S. Gioia

Catálogo-na-publicação

Reis, Livia Bueno
Parametric geometry optimization of an ejector for compression / L. B. Reis -- versão corr. -- São Paulo, 2021.
74 p.

Dissertação (Mestrado) - Escola Politécnica da Universidade de São Paulo. Departamento de Engenharia de Minas e de Petróleo.

1.Computational fluid dynamics 2.ejector 3.parametric geometry optimization 4.shape optimization I.Universidade de São Paulo. Escola Politécnica. Departamento de Engenharia de Minas e de Petróleo II.t.

Nome: REIS, Livia Bueno

Título: Parametric geometry optimization of an ejector for compression

Título em português: Otimização paramétrica de geometria de um ejetor para compressão

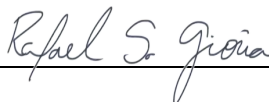
Dissertação apresentada ao Departamento de Engenharia de Minas e de Petróleo da Escola Politécnica da Universidade de São Paulo para obtenção do título de Mestre em Ciências.

Aprovado em: 06 de maio de 2021

Banca Examinadora

Prof. Dr. Rafael dos Santos Gioria
Instituição: Escola Politécnica da USP - PMI
Julgamento: Aprovado

Assinatura:



Dr. Ivan Korkischko
Instituição: IPEN
Julgamento: Aprovado

Assinatura:



Dra. Daiane Iglesia Dolci
Instituição: Escola Politécnica da USP – PME
Julgamento: Aprovado

Assinatura:



*À pesquisa brasileira e aos que se dedicam
diariamente para o reconhecimento e a
valorização da ciência no país.*

ACKNOWLEDGMENTS¹

Agradeço aos meus pais, Nilvanda e Honorato, e ao meu irmão, João Victor, pelo apoio constante às minhas decisões e por acreditarem em mim e me incentivarem.

À minha família, em especial aos meus avós, por todo o carinho e amor que renovam minhas energias a cada dia.

Às minhas amigas Lara, Micaela e Nicole, por compartilharem estes 25 anos de vida e amizade e estarem comigo em mais esta etapa.

Ao Ricardo, pelo companheirismo e carinho, por ler e criticar meus textos, e por me dar o suporte que eu precisava na difícil tarefa de desenvolver um mestrado durante uma pandemia.

Aos meus amigos da pós-graduação, especialmente a Nathália, Paulo, Mayara e Marum, por todas as discussões enriquecedoras e, também, pela descontração nos nossos momentos de balbúrdia.

Ao Rafael Gioria, meu orientador, por todo o apoio, orientação e atenção e pelos conhecimentos compartilhados, essenciais para o desenvolvimento desta pesquisa.

Aos professores e funcionários de Engenharia de Petróleo da EPUSP em Santos, pela contribuição indispensável na minha formação durante o mestrado e por toda dedicação e troca de conhecimento.

Agradeço o apoio da FAPESP e SHELL Brasil por meio do '*Research Centre for Gas Innovation - RCGI*' (Proc. FAPESP 2014/50279-4), sediado na Universidade de São Paulo, e o apoio dado pela ANP (Agência Nacional do Petróleo, Gás Natural e Biocombustíveis) através da regulamentação de P&D.

A FAPESP (Proc. 2019/05197-3) pelo financiamento da bolsa de mestrado referente à pesquisa realizada neste trabalho.

¹ Written in Portuguese.

ABSTRACT

Ejectors have wide industrial application and the improvement in their efficiency is sought to increase the viability of their use. This study performs the optimization of the entire geometry of a liquid jet liquid (LJL) ejector with multiple parameters to maximize energy efficiency. The approach with multiple parameters allows to identify key geometrical features and interdependent parameters, like nozzle position and mixing chamber length, with respect to performance. Computational fluid dynamics (CFD) and optimization simulations were performed to optimize the parameters of Bézier curves that characterize the device's geometry. The optimization results showed that the ejector efficiency curve is sensitive to the nozzle and the suction chamber geometries. Simulations that consider the nozzle diameter and the nozzle position along ejector axis (NXP) as parameters of the optimization process resulted in higher efficiency values than those that kept these parameters fixed. The optimization of the diffuser curve, including the diameter of the diffuser and the length of the mixing chamber, also contributed to increase the efficiency of the device. It was observed that the increase in the length of the mixing chamber and the spacing of the nozzle imply similar effects in the efficiency and in the pressure, velocity and energy dissipation rate profiles confirming some correlation of these parameters on the performance. One may observe the effect of geometry modification through optimization on the flow profiles in key sections of the ejector: the flow profiles in the optimized geometry tend to be more homogenous, hence less dissipative, and it is also confirmed by local energy dissipation rate.

Keywords: Computational fluid dynamics, ejector, parametric geometry optimization, shape optimization

RESUMO

Os ejetores possuem ampla aplicação industrial e as melhorias em sua eficiência buscam aumentar a viabilidade de seu uso. Este estudo realiza a otimização de toda a geometria de um ejetor de líquido (*Liquid jet liquid* - LJJ) com múltiplos parâmetros para maximizar a eficiência energética. A abordagem com vários parâmetros permite identificar as principais características geométricas e parâmetros interdependentes, como a posição do bocal e o comprimento da câmara de mistura, que influenciam no desempenho do ejetor. Dinâmica de fluidos computacional (CFD) e simulações de otimização foram realizadas para otimizar os parâmetros das curvas de Bézier que caracterizam a geometria do dispositivo. Os resultados da otimização mostraram que a curva de eficiência do ejetor é sensível às geometrias do bocal e da câmara de sucção. Simulações que consideram o diâmetro do bocal e a sua posição ao longo do eixo do ejetor (NXP) como parâmetros do processo de otimização resultaram em valores de eficiência superiores aos que mantiveram esses parâmetros fixos. A otimização da curva do difusor, incluindo o diâmetro do difusor e o comprimento da câmara de mistura, também contribuiu para aumentar a eficiência do dispositivo. Observou-se que o aumento do comprimento da câmara de mistura e do espaçamento entre bocal e câmara de mistura implicam em efeitos semelhantes na eficiência e nos perfis de pressão, velocidade e taxa de dissipação de energia, confirmando alguma correlação desses parâmetros no desempenho. Pode-se observar o efeito da modificação da geometria por meio da otimização nos perfis de fluxo em seções-chave do ejetor: os perfis de fluxo na geometria otimizada tendem a ser mais homogêneos, portanto, menos dissipativos. Isto também é confirmado pelos campos de taxa de dissipação de energia local.

Palavras-chave: Dinâmica de Fluidos Computacional, ejetor, otimização paramétrica de geometria, otimização de forma

LIST OF FIGURES

Figure 1 - Schematic representation of an ejector.....	14
Figure 2 - Schematic diagram of an ejector and its components: nozzle (1), suction chamber (2), mixing chamber (3) and diffuser (4)	18
Figure 3 – Quadratic Bézier curve with points obtained for $m = 0.5$. P_0 and P_2 are the endpoints and P_1 is the control point of the curve.	31
Figure 4 - Ejector base geometry	36
Figure 5 – Axisymmetric ejector geometry	37
Figure 6 - Quadratic Bézier in primary inlet, nozzle, and secondary inlet.....	38
Figure 7 - Quadratic Bézier in diffuser (cases 6, 7 and 8)	38
Figure 8 - Mesh convergence for $M = 3.0$ (a) and $M = 5.5$ (b).....	43
Figure 9 - Mesh details at the mixing chamber inlet	43
Figure 10 - Efficiency curve for simulated base geometry compared to the experimental curve - $M = Q_2/Q_1$. The gray area represents the range $\pm 1 \cdot RMSE$..	45
Figure 11 - Simulated total pressure profiles compared to the profiles obtained by Sanger (1968a)	45
Figure 12 - Original geometry (a) compared to optimized geometry for case 1 (b) and 2 (c)	49
Figure 13 - Ejector efficiency with geometry optimized for $M = 3.0$ and $M = 5.5$ as a function of the entrainment ratio compared to efficiency curve of the base geometry	50
Figure 14 - Base geometry (a) compared to optimized geometries for $M = 5.5$: (b) case 3, (c) case 4 and (d) case 5	52

Figure 15 - Ejector efficiency with geometry optimized for $M = 5.5$ as a function of the entrainment ratio	53
Figure 16 - Comparison of the geometries of case 6 (a), case 7 (b) and case 8 (c)..	55
Figure 17 - Ejector efficiency with geometry optimized for $M = 5.5$ as a function of the entrainment ratio (with parametrized diffuser curve)	56
Figure 18 - Ejector efficiency for base case, case 2 and case 9 as a function of the entrainment ratio	57
Figure 19 - Efficiency curve for cases 5 and 10 (a and b) compared to the base geometry curve.....	58
Figure 20 - Velocity, static pressure and total pressures profiles for base geometry and cases 2, 3, 4 and 5 calculated for $M = 5.5$	60
Figure 21 - Velocity, static pressure and total pressures profiles for base geometry and cases 6, 7 and 8 calculated for $M = 5.5$	62
Figure 22 - Pressure ratio as a function of the entrainment ratio for base geometry, case 5 and case 8	63
Figure 23 - Energy dissipation fields in the region of the mixing section and diffuser inlet for $M = 5.5$	65
Figure 24 - Streamlines for $M = 5.5$ in base case (a), case 5 (b) and case (8).....	66

LIST OF TABLES

Table 1 - Geometric parameters for ejector construction	36
Table 2 – Coordinates of the control points	38
Table 3 - Boundary conditions	39
Table 4 - Optimization parameters and description	40
Table 5 - Lower and upper bounds of optimization parameters. Every parameter is nondimensional except p_8	42
Table 6 - Optimization results for M=3.0 (case 1).....	48
Table 7 - Optimization results for M=5.5 (case 2).....	48
Table 8 - Optimization results for M=5.5 with nozzle diameter optimized (case 3)....	50
Table 9 - Optimization results for M=5.5 with NXP optimized (case 4).....	51
Table 10 - Optimization results for M=5.5 with nozzle diameter and NXP optimized (case 5)	51
Table 11 - Value of parameters and efficiency for case 6	53
Table 12 - Optimization results for M=5.5 with diffuser curve optimized (case 7).....	54
Table 13 - Optimization results for M=5.5 with diffuser curve, nozzle diameter and NXP optimized.....	54
Table 14 - Optimization result for case 9	56
Table 15 - Optimization result for case 10 (a) and (b) using the combined objective function in Eq. (44) which is the sum of the efficiencies for three M values.....	57

CONTENTS

1	INTRODUCTION	13
1.1	Objectives	15
1.2	Justification	15
2	LITERATURE REVIEW	17
2.1	Ejectors	17
2.2	Ejector components and operation process	17
2.3	Ejector applications	19
2.4	Ejector geometry	20
2.5	Experimental studies of ejectors	21
2.6	Computational Fluid Dynamics	23
2.6.1	Governing equations	23
2.6.2	Finite Element Method in CFD	24
2.6.3	$k\omega$ –SST turbulence model	26
2.6.4	CFD applied to ejectors	28
2.7	Bézier curves	29
2.7.1	De Casteljau Algorithm	30
2.7.2	Bernstein's polynomials	31
2.8	Optimization and Nelder-Mead method	32
3	METHODOLOGY	36
3.1	Ejector geometry definition	36
3.2	Computational set-up	38
3.3	Optimization set-up	40
3.3.1	Control variables and parameters	40
3.3.2	Objective function	41
3.3.3	Constraints	41
3.4	Mesh convergency	42
3.5	Validation of the simulations	44
3.6	Evaluated cases	46
4	RESULTS AND DISCUSSIONS	48
4.1	Influence of the entrainment ratio (M) used in the optimization	48
4.2	Effect of nozzle and NXP optimization	50
4.3	Effect of parameterization and optimization of the diffuser boundary	53

4.4	Effect of inlet diameters optimization.....	56
4.5	Effect of optimization for simultaneous M values	57
4.6	Influence of geometries on pressure and velocity profiles.....	58
4.7	Effect of optimizations on pressure ratio	63
4.8	Influence of geometries on energy dissipation rate fields.....	63
5	CONCLUSIONS.....	67
5.1	Suggestions for future research	68
6	REFERENCES.....	69

1 INTRODUCTION

The global warming and the increase in the concentration of atmospheric CO₂ (carbon dioxide) are a growing global concern. This problem is associated with industrial and technological development, as well as population growth, which explain the increasing demand for energy sources. The combustion of fossil fuels, one of the main energy resources of today, is responsible for the majority of greenhouse gas emissions associated with human activities (REDDICK; SORIN; RHEAULT, 2014).

Carbon Capture and Storage (CCS), practice that involves capturing of carbon dioxide from power plants, industrial facilities and natural gas wells, and transporting it to a favorable geological site for permanent storage, has been recognized as the most promising method to reduce CO₂ emissions and mitigate climate changes (RAZA et al., 2019). One of the biggest costs of CCS systems is the capture process, which includes the gas compression. The gas compression is performed to facilitate both transport and storage (IPCC, 2006).

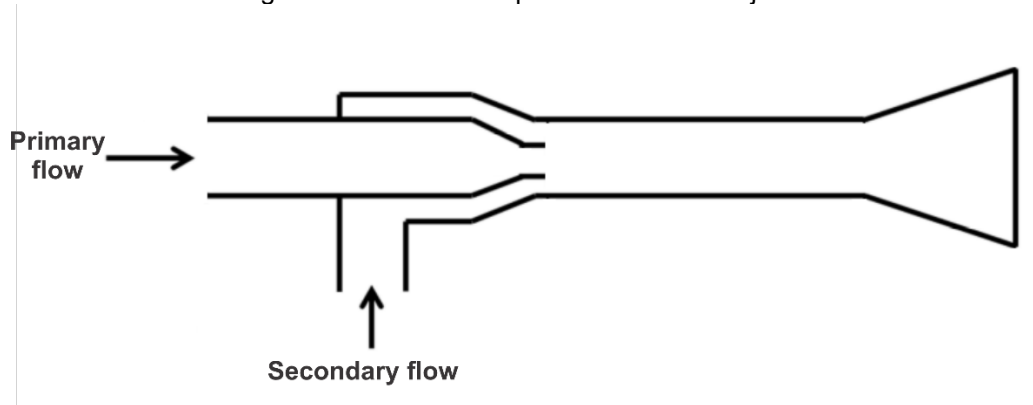
Due to the high cost, it is necessary to develop new gas compression technology and to improve existing ones. In this context, ejectors have potential applicability in initial stages of CO₂ compression systems for CCS application (CUNNINGHAM, 1974; TASHTOUSH; AL-NIMR; KHASAWNEH, 2019).

Ejectors (Figure 1), or jet pumps, are mechanical devices that use momentum of a motive fluid to suction another fluid, called the secondary flow. The motive fluid can be composed of a liquid or gaseous stream, while the moved fluid can be gas, liquid, gas-liquid mixture or solids. The multiphase flow ejector has very complex physics, hence the present work focus on the study of the incompressible flow ejector as a proof of concept of efficiency optimization application and its impact in flow physics.

Ejectors are widely used mainly due to high reliability (absence of moving parts that does not require constant maintenance) and adaptability to installation in remote or inaccessible locations. In addition, the ejectors have small dimensions, which implies a great advantage in terms of cost (CUNNINGHAM, 1974). On the other hand, the low energy efficiency of the ejectors caused by friction losses and the fluid mixing process is one of the main disadvantages of these equipment (DROZDOV et al., 2011).

Therefore, the study of ejectors is, in most cases, focused on increasing their efficiency, to improve, consequently, the efficiency of the systems in which the ejectors are inserted.

Figure 1 - Schematic representation of an ejector



Source: (PEDROSO, 2015 - Adapted)

The efficiency of the ejector depends on many factors, such as the pressure upstream of the nozzle and in the suction chamber and geometric parameters. The optimization of the geometry of the ejectors is a path to improve the energy efficiency. Several studies have investigated the effect of ejector geometry on its efficiency, through the study of parameters like area ratio, setback distance, mixing tube length, and shape of the driving nozzle (MALLELA; CHATTERJEE, 2011; PALACZ et al., 2016; PEDROSO, 2015; VARGA et al., 2011; VARGA; OLIVEIRA; DIACONU, 2009; YAPICI; ALDAŞ, 2013; ZHU et al., 2009). However, these studies involve cases of parametric sweeping of each geometric variables of the ejector individually. Optimization algorithms and simultaneous evaluation of parameters are not widely used resources and it is a key contribution of the present work.

Another gap found in the study of Liquid jet liquid (LJL) ejectors is the existence of few experimental studies with enough data and information to validate numerical simulations. Research of liquid ejectors with computational fluid dynamics (CFD) are validated with old experimental works, due to this lack of data (MARUM et al., 2021; PEDROSO, 2015; YAPICI; ALDAŞ, 2013). In this context, the present work uses Sanger (1968a) as a basis for validation, which presents complete information on geometry, pressure measurements and efficiency calculations.

Liquid jet liquid ejectors are applied in district heating and cooling systems (LIU; ZHAN; LIA, 2017; WANG; WANG, 2019). In addition, there are important applications

in the oil industry, in boiling water reactors and fish locomotion (CUAMATZI-MELÉNDEZ; FLORES-CUAMATZI, 2020; MANGIALARDO et al., 2014; XU et al., 2017, 2019, 2020; YAN et al., 2018).

Computational fluid dynamics technique is used in the analysis and study of ejector performance and in the computational modeling of the equipment. The technique has been widely used to investigate the effects of important parameters of the geometry on the ejector performance (VARGA; OLIVEIRA; DIACONU, 2009; ZHU et al., 2009). Simulations in CFD are also used in the study of ejector geometry components optimization (PALACZ et al., 2016).

In this study, computational fluid dynamics simulations combined to the Nelder–Mead optimization technique (NELDER; MEAD, 1965) were performed to optimize the parameters of the Bézier curves that characterize the geometry of a water ejector. For the development of the project, an incompressible fluid flow model was considered.

1.1 Objectives

The main objective of this work is the development of a geometry optimization of the ejector curves to maximize its efficiency. It was intended to analyze the influence of some geometric parameters, such as section diameters and component length, and operational conditions on the ejector efficiency.

In addition, dynamic fluid characteristics of the ejector, such as pressure and velocity profiles and dissipation energy rate fields, were evaluated to analyze the influence of optimizations on fluid flow and to identify the flow physics that are affecting the performance for a given geometry.

1.2 Justification

The research presented in this dissertation is part of Project 38 - High efficiency ejector for gas compression of the Research Center for Gas Innovation - RCGI (FAPESP Proc. 2014 / 50279-4).

The final objective of Project 38 is to test the feasibility of using gas-liquid (multiphase) ejectors in Carbon Capture and Storage (CCS) processes, through the development of the evaluation of the limits of the existing technology in gas

compression using these ejectors. Ejectors are potentially useful in the early stages of CO₂ compression, if high performance (efficiency) is achieved.

The current Master thesis fitted in Project 38, which it was intended to identify the main geometric characteristics that most affect the efficiency of the ejector and to develop geometry optimization methodologies through different techniques: parametric, shape and topological. Given the complexity of the physics involved in multiphase ejectors, the model chosen as a reference was the incompressible ejector (liquid-liquid ejector), for a focus on improving efficiency and not dealing with multiphase flow modeling.

In this context, the present master's work focused on the incompressible flow ejector as a proof of concept in application of geometry optimization, through parametric curves, to increase the energy efficiency of the device and evaluate its impact on the flow of fluids.

2 LITERATURE REVIEW

2.1 Ejectors

Ejectors, or jet pumps, are devices that perform their pumping action by the transfer of energy from a high-velocity jet to one of low velocity (MALLELA; CHATTERJEE, 2011). They use the pressure energy of a second fluid as a driving force. Such devices are generally simple to set up, with no moving parts, high operational robustness and simplicity of installation (PEDROSO, 2015).

Basically, an ejector is a flow device with two inlets and a discharge that allows the primary stream to entrain the secondary low-pressure stream. The two flows are mixed inside the device and discharged at some intermediate pressure. Thus, the pumping provided by the ejector has as its operating principle the generation of vacuum necessary to create the suction, through the acceleration of the primary flow through a nozzle (TASHTOUSH; AL-NIMR; KHASAWNEH, 2019).

A common classification for ejectors is given in relation to the motive fluid (primary) and the moved fluid (secondary), as below (PEDROSO, 2015):

- LJJ – Liquid Jet Liquid: ejector which both primary and secondary fluids are in liquid state;
- LJG - Liquid Jet Gas: ejector which primary fluid is in liquid phase and secondary fluid is a gas phase;
- LJGL - Liquid Jet Gas-Liquid: ejector with a liquid phase as the primary fluid and a two-phase liquid-gas mixture as the secondary fluid.

The present work focuses on the study of the incompressible flow ejector (LJJ ejector) for an analysis of the application of efficiency optimization and its impact on the fluid dynamic characteristics of the flow.

2.2 Ejector components and operation process

Figure 2 shows a schematic representation of an ejector and its four basic components: nozzle (1), suction chamber (2), mixing chamber (3) and diffuser (4).

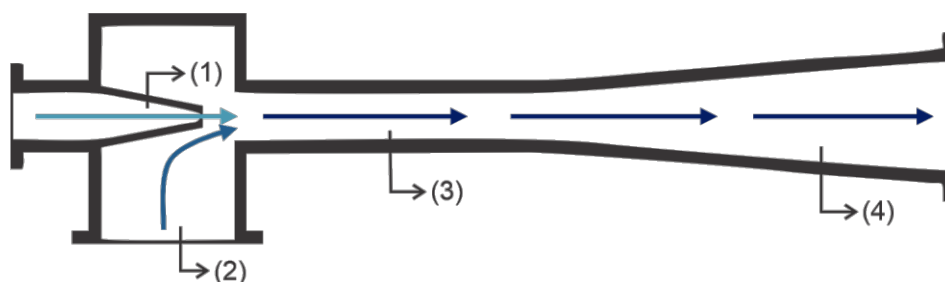
The nozzle is one of the main structural elements of the ejector. This component acts as a converter of potential energy into kinetic energy and creates a particular distribution of turbulence in the jet.

The suction chamber supplies the injected fluid to the jet of power fluid. The entry of the secondary fluid into the primary stream can occur at various angles. For an axisymmetric ejector configuration, for example, the suction chamber and the nozzle are concentric.

The mixing section (throat) is where mixing and equalizing the velocity field of two flows occurs. The mixing chamber must promote the complete mixing between primary and secondary fluids and create a uniform velocity profile for the entrance of this mixture in the diffuser. However, the throat cannot be too long, to minimize friction losses in the ejector. For these reasons, the mixing section length is a parameter of great importance in the design of an ejector and in the efficiency evaluation.

The diffuser acts as a converter of the total kinetic flow into potential energy by gradually reducing the speed. The variation of the cross-sectional area characterizes the geometry of a diffuser.

Figure 2 - Schematic diagram of an ejector and its components: nozzle (1), suction chamber (2), mixing chamber (3) and diffuser (4)



The ejector operation process is simple and does not require external energy interactions. The primary fluid is accelerated through the nozzle (1) into a region containing the secondary fluid. The fall in pressure at the nozzle exit induces the flow of the secondary fluid, through the suction chamber (2), in the direction of the primary stream. The secondary fluid is entrained and carried forward into a mixing chamber (3). The jet expands and there is a transfer of energy and momentum from the primary to the secondary fluid through a process of turbulent mixing. At the end of the mixing chamber, momentum exchange should be complete and the mixed fluid is discharged,

often through a diffuser (4) which is used for further static pressure recovery (ESDU, 1986).

2.3 Ejector applications

As already mentioned, ejectors are devices capable of pumping fluids (secondary fluid) using energy from another fluid (primary fluid). As the working fluid can be liquid or gas, the application potential of the use of ejectors is wide and covers several industrial sectors.

In oil and gas industry, ejectors are applied to improve the production, contributing to the lifting process of the fluids produced in the wells. Sarshar (2012) cites applications in oil and gas fields, which include: installation of an ejector to decrease the flowing tubing head pressure (FTHP), using recycled gas as a high-pressure fluid; use of gas from high-pressure wells to power a jet pump, allowing the reduction of back pressure in a line that serves low-pressure satellite wells; replacement of first stage compressor with a jet pump in onshore systems. The main benefits of applying ejectors in these cases are the better use of available energy, minimal maintenance requirements, as they have no moving parts and no emissions to the atmosphere (SARSHAR, 2012).

In post-combustion carbon capture in electric power, the use of ejector is studied to upgrade external waste heat for the purpose of reducing the amount of valuable turbine steam that is required to supply the solvent regeneration process (REDDICK; SORIN; RHEAULT, 2014). Ejectors are also applicable for gas compression (CUNNINGHAM, 1974; TASHTOUSH; AL-NIMR; KHASAWNEH, 2019), which is a process that facilitates the transport and storage of CO₂, and is one of the biggest costs of CCS systems (IPCC, 2006).

A common application of ejectors, which concentrates many studies focused on analyzing and increasing the performance of the device, is in refrigeration systems (AIDOUN; OUZZANE, 2004; CUI; QIAN; YU, 2020; LAWRENCE; ELBEL, 2013; LUCAS; KOEHLER, 2012). Refrigeration systems with ejectors are an alternative to traditional technologies that use compressors due to their reliability, limited maintenance needs and low initial and operating costs (BESAGNI; MEREU; INZOLI, 2016).

Recent studies have shown applications of ejectors as an exhaust gas recirculation device for fuel cells, to improve fuel utilization and extend the life of proton exchange membrane cells, especially in automotive applications (LIU; TU; CHAN, 2021). Other applications, such as in desalination processes (LIU et al., 2019) and trigeneration system for dairy applications (VUTUKURU; PEGALLAPATI; MADDALI, 2019), are also found in the literature.

Liquid jet liquid (LJL) ejectors applications are found in district heating and cooling systems (LIU; ZHAN; LIA, 2017; WANG; WANG, 2019). In the heating system, the LJL ejector offers energy saving advantages compared to the heat exchanger and water mixer, improve the temperature difference between supply and return water of the primary network, and increase the heat exchange effect (LIU; LI; ZENG, 2017; LIU; ZHAN; LIA, 2017). A scheme of applying the jet pumps can be used to enhance the hydraulic balance of the district pipe network in district cooling systems, replacing throttle valves that are difficult to adapt to dynamic regulations (WANG; WANG, 2019).

In the oil industry, the application of LJL ejectors has been studied to replace gate valves in water injector wells, with the aim of reducing energy consumption on offshore platforms (YAN et al., 2018).

Other applications of the incompressible ejectors are, for example, in boiling water reactor (CUAMATZI-MELÉNDEZ; FLORES-CUAMATZI, 2020; MANGIALARDO et al., 2014) and fish locomotion (XU et al., 2017, 2019, 2020).

2.4 Ejector geometry

Ejectors have a simple structure and no moving parts. Therefore, they have a long lifespan and little maintenance, as well as low costs. However, for the ejector to be economically attractive, it is necessary to improve its performance (VARGA; OLIVEIRA; DIACONU, 2009).

Several studies have investigated the effect of ejector geometry on its efficiency. The geometric parameters influence the velocity of the primary and secondary flows, the mixture of the two fluids, the pressures along the equipment and, consequently, the efficiency of the ejector.

Zhu et al. (2009) investigated the effects of two important ejector geometry parameters: the primary Nozzle Exit Position (NXP) and the mixing section converging angle, on its performance. The study showed that optimum primary nozzle position or converging angle cannot be predefined to meet all operating conditions. When the operating conditions are different from the design point, both parameters should be adjusted accordingly to maximize the ejector performance.

In their study, Varga; Oliveira; Diaconu (2009) consider three geometrical factors in the evaluation of the ejector's performance: the area ratio between the nozzle and constant area section (mixing chamber), nozzle exit position (NXP) and constant area section length. The results indicated that the existence of ideal geometric parameters depends on the operating conditions, such as the entrainment ratio and critical back pressure.

Numerical simulations were carried out by Mallela; Chatterjee (2011) to determine the effects of area ratio, setback distance, mixing tube length, and shape of the driving nozzle on the performance of the jet pump. The study identified reasons that account for major losses taking place when primary and secondary fluids meet and the dependence of these losses on ejector geometry.

In a study of an ejector-based multi-evaporator refrigeration cycle, Yan, Li and Liu (2020) sought, through CFD simulations, to find the ideal primary nozzle throat diameter, optimize the primary nozzle geometry of the convergent and convergent-divergent nozzle with fixed NXP, ejector performance difference between convergent nozzle and the convergent-divergent nozzle and analyze the effect of varied NXP on the geometric parameters of the optimized nozzle and on the ejector performance.

In the cases, the geometric parameters are evaluated individually, through parametric scans and without the use of an optimization algorithm.

2.5 Experimental studies of ejectors

Experimental studies of ejectors generally have a high cost, as they require investments in the construction of the device and in the installation of equipment for experimental tests. The high costs and the complexity of assembling the test limit the experimental work to a few study geometries. However, numerical models such as

CFD models, despite their advantages, require experimental results to validate their analysis through comparisons of results.

An experimental investigation of a miniature ejector (about 140 mm in total length) was carried out by Dong et al. (2019). The study looked at an ejector with water as a working fluid in a cooling system used to maintain the temperature of an electric chip. The experiments were carried out to test the effects of working conditions, the position of the NXP and area ratio on the coefficient of performance (COP). The experimental test setup consisted of high-temperature and low-temperature evaporators, the prototype miniature steam ejector, a condenser, a transparent reservoir, a cooling bath, two electric heaters, two transformers, and measuring devices. The results determined the temperature and pressure ranges of the ejector, as well as the ideal NXP value for a maximum COP and the effect of the area ratio.

Lima Neto (2011) carried out an experimental study on water ejectors with different diameters. The nozzle-to-throat area ratios were also evaluated, and the results revealed the importance of this parameter to characterize the maximum suction lift of the ejector. A centrifugal pump that distributes water from a feed tank to the ejector and a suction tank, from which the secondary fluid is lifted, make up the set-up of the experiment.

Some numerical studies present experimental tests carried out by the authors themselves, to validate their computational models (YAN; LI; LIU, 2020; ZHU et al., 2009). Yapici and Aldas (2013), in turn, uses experimental data presented in a doctoral thesis to compare and validate his CFD model.

Most of the experimental studies found in the literature do not provide a complete detail of the ejector geometry, parameters, and conditions of the experimental tests. In this sense, the works published by Sanger (1968a, 1968b, 1970), despite being older, present more complete and detailed data. The present work will use the experimental data of Sanger (1968a) to carry out the validations. The experimental study of Sanger (1968a) evaluated the non-cavitation and cavitation performance of two jet pumps with nozzle-to-throat area ratios of 0.066 and 0.197 in a water facility.

2.6 Computational Fluid Dynamics

Computational Fluid Dynamics is defined as the set of techniques that allow numerical simulations of fluid flows through computers. In CFD, the laws that govern the movement of fluids, inside or around a material system, are solved numerically by the computer and their geometry is also modeled on the computer (HIRSCH, 2007).

The computational fluid dynamics makes it possible to predict the concentration fields, velocities, pressure, temperatures and turbulent flow properties, through models based on the principles of conservation of mass, energy and momentum, in the space and time domain (ANDERSON JR. et al., 2009).

2.6.1 Governing equations

The equations that govern the movement of fluids represent mathematical statements of the conservation laws of physics, which are mass conservation, Newton's second law and energy conservation.

With the application of the principles of conservation of mass in a fluid particle, the continuity equation is given by equation (1). The first term is the rate of change in time of the density (mass per unit volume) and the second describes the net flow of mass out of the element across its boundaries and is called the convective term. (VERSTEEG; MALALASEKERA, 2007):

$$\frac{\partial \rho}{\partial t} + \nabla \cdot (\rho \cdot \mathbf{u}) = 0 \quad (1)$$

where:

ρ is the fluid density;

\mathbf{u} is the velocity vector;

t is the time.

For incompressible fluids, such as those considered in this work, the density is constant, and the continuity equation becomes:

$$\rho \nabla \cdot \mathbf{u} = 0 \quad (2)$$

Applying Newton's 2nd law, we obtain the momentum conservation equation (equation 3), also known as the Navier Stokes equation (HIRSCH, 2007).

$$\rho \frac{\partial \mathbf{u}}{\partial t} + \rho(\mathbf{u} \cdot \nabla)\mathbf{u} = -\nabla p + \mu \left[\Delta \mathbf{u} + \frac{1}{3} \nabla(\nabla \cdot \mathbf{u}) \right] + \rho \mathbf{f}_e \quad (3)$$

where:

p is the static pressure;

μ is the dynamic viscosity;

\mathbf{f}_e is the external force vector.

For incompressible fluids, which satisfy equation (2), equation (3) is reduced to:

$$\rho \frac{\partial \mathbf{u}}{\partial t} + \rho(\mathbf{u} \cdot \nabla)\mathbf{u} = -\nabla p + \mu \Delta \mathbf{u} + \rho \mathbf{f}_e \quad (4)$$

The governing equations of fluid movements are partial differential equations. The analytical resolution of these equations is limited to simple cases of fluid flow. Therefore, numerical methods are used to obtain approximate solutions to these equations, typically based upon different types of discretization. In this work, the COMSOL Multiphysics software was used, which uses a finite element method approach.

2.6.2 Finite Element Method in CFD

One of the numerical techniques used to solve partial differential equations is the finite element method (FEM). FEM is characterized by the subdivision of a continuous domain into elements, which form a grid. In addition to the elements, the geometry discretized in the FEM presents nodal points, or simply nodes. Nodal points are typical points of elements such mid-side points and mid-element points. (ANDERSON JR. et al., 2009).

This numerical technique has some essential and advantageous characteristics in addressing some problems, such as:

- The grid formed by the finite elements does not need to be structured and the elements can be curved. With unstructured grids, complex geometries can be manipulated with ease, because no implicit structure of coordinate lines is imposed by the grid and the mesh can be concentrated where it is necessary, saving computer storage (ANDERSON JR. et al., 2009; VERSTEEG; MALALASEKERA, 2007).

- The solution representation is strongly linked to the geometric representation of the domain. The solution of the discrete problem is assumed a priori as having a prescribed form and is built by the variation of function between values at nodal points (ANDERSON JR. et al).
- The method is easy to obtain higher order accuracy and implementation of the boundary conditions, since it does not seek the solution of the PDE itself but seeks the solution of an integral form of the PDE, usually obtained from a weighted residual formulation (ANDERSON JR. et al).
- The method is discretized in a modular way. Discrete equations are built from contributions at the element level that are then assembled (ANDERSON JR. et al).

The finite element method looks for an approximate solution that belongs to a finite dimension function space and that has the form (ANDERSON JR. et al., 2009):

$$u \approx \hat{u} = \psi + \sum_{k=1}^N \phi_k u_k \quad (5)$$

where:

\hat{u} is an approximation to the solution u of differential equation f ;

ψ is a function which satisfies the boundary conditions;

ϕ_k are the basis functions;

N is dimension of the basis functions space.

Since the function \hat{u} is an approximation of the solution of the differential equation denoted by $a(u) = f$, a residual is left, represented by the following equation:

$$r_\Omega = a(\hat{u}) - f \quad \text{in } \Omega \quad (6)$$

An approximate solution to the problem is obtained by finding a way to make this residual as close to zero as possible. In the finite element method, this is done by requiring that an appropriate number of weighted integrals of the residual over Ω be zero, which is called the weighted residual method.

$$\int_{\Omega} w_i r_{\Omega} d\Omega = 0; \quad i = 1, 2, \dots, N \quad (7)$$

Where $W = \{w_i; i = 1, 2, \dots, N\}$ is a set of weighting functions.

The choice of the weight function w_i depends on the weighting criterion to be used. The most popular choice for the weighting functions in the finite element method are the base functions themselves, which characterizes the Galerkin method (ANDERSON JR. et al).

The momentum equation can easily become unstable if discretized using Galerkin finite element method and stabilized finite element methods are generally necessary to obtain physical solutions. Therefore, COMSOL uses the Galerkin least squares (GLS) (HAUKE; HUGHES, 1993) applied to the Navier-Stokes equations (COMSOL MULTIPHYSICS, 2017).

2.6.3 $k\omega$ –SST turbulence model

The turbulence models are based on the Reynolds-averaged Navier-Stokes (RANS) equations, which is the most commonly type used in industrial flow applications (COMSOL MULTIPHYSICS, 2017).

For an incompressible and Newtonian fluid, the Navier-Stokes equations take the form:

$$\rho \frac{\partial \mathbf{u}}{\partial t} + \rho(\mathbf{u} \cdot \nabla)\mathbf{u} = \nabla \cdot [-p\mathbf{I} + \mu(\nabla\mathbf{u} + (\nabla\mathbf{u})^T)] + \mathbf{F} \quad (8)$$

$$\rho \nabla \cdot \mathbf{u} = 0 \quad (9)$$

where:

\mathbf{F} is the external force.

The Reynolds-averaged representation of turbulent flows divides each property (ϕ) into an averaged value ($\bar{\phi}$) plus a fluctuating part (ϕ'):

$$\phi = \bar{\phi} + \phi' \quad (10)$$

Reynolds-averaged Navier-Stokes (RANS) equations are given by decomposition of the flow field into an averaged part and a fluctuating part and insertion into the Navier-Stokes equation, as in equation 10:

$$\rho \frac{\partial \mathbf{U}}{\partial t} + \rho \mathbf{U} \cdot \nabla \mathbf{U} + \nabla \cdot (\overline{\rho \mathbf{u}' \times \mathbf{u}'}) = -\nabla P + \nabla \cdot \mu (\nabla \mathbf{U} + (\nabla \mathbf{U})^T) + \mathbf{F} \quad (11)$$

$$\rho \nabla \cdot \mathbf{U} = 0 \quad (12)$$

where \mathbf{U} is the averaged velocity field.

Turbulence models are closure for RANS equations. The $k\omega$ -SST (Shear Stress Transport) turbulence model (MENTER, 1993, 1994) interpolates between the $k\omega$ and $k\epsilon$ models, combining the characteristics of superior behavior in near-wall region of the $k\omega$ model with the robustness of the $k\epsilon$.

The model equations, with the formulation used by Comsol Multiphysics (2017), are presented below in terms k (turbulent kinetic energy) and ω (specific dissipation rate):

$$\rho \frac{\partial k}{\partial t} + \rho \mathbf{u} \cdot \nabla k = P - \rho \beta_0^* k \omega + \nabla \cdot ((\mu + \sigma_k \mu_T) \nabla k) \quad (13)$$

$$\rho \frac{\partial \omega}{\partial t} + \rho \mathbf{u} \cdot \nabla \omega = \frac{\rho \gamma}{\mu_T} P - \rho \beta \omega^2 + \nabla \cdot ((\mu + \sigma_\omega \mu_T) \nabla \omega) + 2(1 - f_{v1}) \frac{\rho \sigma_\omega \omega^2}{\omega} \nabla \omega \cdot \nabla k \quad (14)$$

Where,

$$P = \min(P_k, 10\rho\beta_0^*k\omega) \quad (15)$$

$$P_k = \mu_T \left(\nabla \mathbf{u} : (\nabla \mathbf{u} + (\nabla \mathbf{u})^T) - \frac{2}{3} (\nabla \cdot \mathbf{u})^2 \right) - \frac{2}{3} \rho k \nabla \cdot \mathbf{u} \quad (16)$$

The turbulent viscosity (μ_T) is given by

$$\mu_T = \frac{\rho \alpha_1 k}{\max(\alpha_1 \omega, S f_{v2})} \quad (17)$$

S is the characteristic magnitude of the mean velocity gradients,

$$S = \sqrt{2S_{ij}S_{ij}} \quad (18)$$

The model constants are defined through interpolation of appropriate inner and outer values,

$$\phi = f_{v1}\phi_1 + (1 - f_{v1})\phi_2 \quad \text{for } \phi = \beta, \gamma, \sigma_k, \sigma_\omega \quad (19)$$

f_{v1} and f_{v2} are the interpolation functions defined as,

$$f_{v1} = \tanh(\theta_1^4) \quad (20)$$

$$\theta_1 = \min \left[\max \left(\frac{\sqrt{k}}{\beta_0^* \omega l_w}, \frac{500\mu}{\rho \omega l_w^2} \right), \frac{4\rho\sigma_{\omega 2}k}{CD_{k\omega} l_w^2} \right] \quad (21)$$

$$CD_{k\omega} = \max \left(\frac{2\rho\sigma_{\omega 2}}{\omega} \nabla \omega \cdot \nabla k, 10^{-10} \right) \quad (22)$$

$$f_{v2} = \tanh(\theta_2^2) \quad (23)$$

$$\theta_2 = \max \left(\frac{2\sqrt{k}}{\beta_0^* \omega l_w}, \frac{500\mu}{\rho \omega l_w^2} \right) \quad (24)$$

where l_w is the distance to the closest wall.

The default model constants are given by,

$$\beta_1 = 0.075, \beta_2 = 0.0828, \beta_0^* = 0.09, \gamma_1 = \frac{5}{9}, \gamma_2 = 0.44,$$

$$\alpha_1 = 0.31, \sigma_{k1} = 0.85, \sigma_{k2} = 1.0, \sigma_{\omega 1} = 0.5, \sigma_{\omega 2} = 0.856$$

2.6.4 CFD applied to ejectors

CFD is a faster and less costly tool when compared to experimental studies, which allows the analysis of different geometries (PEDROSO, 2015). In addition, it allows knowledge of the pressure and velocity fields and other fluid characteristics, which can enrich ejectors studies.

Computational fluid dynamics is widely used in the analysis of ejectors and the study of their performance. Su; Agarwal (2015) conducted numerical simulations to investigate the detailed flow field within a supersonic vapor ejector (water vapor being the working fluid). Liu et al. (2017) used an axisymmetric computational fluid dynamics model to investigate the effect of the area ratio on the efficiencies of the ejector components. Hedges; Hill (1974) developed a method, used to predict results of experimental tests, using the finite difference model of the flow field inside the ejector, based on conservation equations.

In addition to the studies cited, several works use computational fluid dynamics to investigate the effects of various geometric parameters on the ejector performance, such as: suction chamber geometry (YADAV; PATWARDHAN, 2008), nozzle exit position (MALLELA; CHATTERJEE, 2011; RIFFAT; GAN; SMITH, 1996; VARGA et al., 2011; VARGA; OLIVEIRA; DIACONU, 2009; ZHU et al., 2009) and nozzle geometry (MALLELA; CHATTERJEE, 2011; VARGA et al., 2011). The use of CFD to evaluate the effects of geometric parameters is often linked to the optimization studies.

2.7 Bézier curves

In the present study, Bézier curves were chosen to build the geometry of a water ejector and to evaluate the importance of this geometry in the equipment's efficiency. A set of curves connected to each other will be used. Bézier curves were chosen because they are parameterized and readily available in CAD softwares, being appropriate for calculations and sensitivity analysis in the optimization loop.

Bézier curves, initially developed to model the aerodynamic shapes of modern cars, have numerous applications in computer graphics software (FARIN, 1992). These curves are extremely useful for modeling projects and adapt easily to computer systems (SIMONI, 2005).

Bézier curves are parametric curves defined in the interval $[0, 1]$. These curves have points in space that are their controlling parameters. Each of these points has an influence on the curve. A Bézier curve of degree "n" has "n + 1" points for its definition (SIMONI, 2005).

The most used form of Bézier curves is the third degree (Cubic Bezier Curves). Four points define Bézier's cubic: 2 endpoints and 2 control points. The curve necessarily passing through the endpoints and not passing through the control points, but these define its shape (SIMONI, 2005). However, in this study, second order curves (Quadratic Bézier Curves) have been used so far. Two endpoints, which correspond to the beginning and end of the curve, and one control point define a Quadratic Bézier Curve.

Bézier curves can be defined as a set of points found through the Casteljau Algorithm or explicitly according to Bernstein's polynomials.

2.7.1 De Casteljau Algorithm

The De Casteljau algorithm is the fundamental algorithm that supports the construction and calculation of Bézier curves (FARIN, 1992; PRAUTZSCH; BOEHM; PALUSZNY, 2002; SIMONI, 2005).

Let them be $P_0, P_1, \dots, P_n \in \mathbb{R}^3$ and $m \in \mathbb{R}$, we have the equation (1):

$$P_i^r(m) = (1 - t)P_i^{r-1}(m) + mP_{i+1}^{r-1}(m) \begin{cases} r = 1, 2, \dots, n \\ i = 0, 1, \dots, n - 1 \end{cases} \quad (25)$$

where $P_i^0(m) = P_i$.

$P_0^n(m)$ is a point for a given value of parameter m on the Bézier curve. The set of points $P_0^n(m)$ define the Bézier curve of degree n , $B^n(m)$, as shown in equation (2).

$$B^n(m) = \{P_0^n(m); m \in [0, 1]\} \quad (26)$$

The equations (3), (4), (5) and (6) represent the Bézier's quadratic, using the De Casteljau algorithm:

$$P_0^2(m) = (1 - m)P_0^1(m) + mP_1^1(m) \quad (27)$$

$$P_0^1(m) = (1 - m)P_0 + mP_1 \quad (28)$$

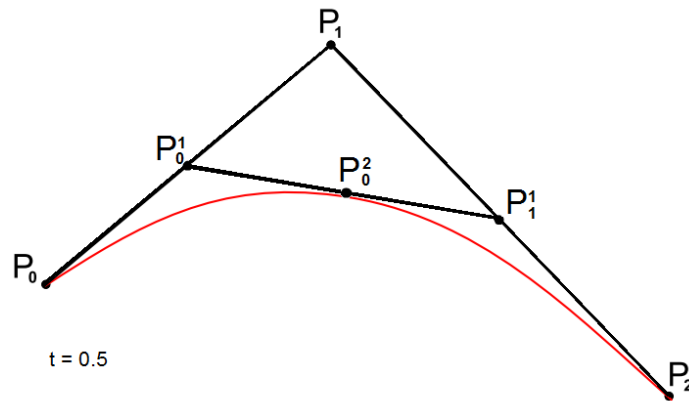
$$P_1^1(m) = (1 - m)P_1 + mP_2 \quad (29)$$

Equation (6) results from the replacement of equations (4) and (5) in (3) and it is the equation that represents the quadratic Bézier curves:

$$B^2(m) = P_0^2(m) = (1 - m)^2P_0 + 2m(1 - m)P_1 + m^2P_2 \quad (30)$$

Figure 3 illustrates a quadratic Bézier curve, in which the points P_0^1 , P_1^1 and P_0^2 were plotted for $m = 0.5$.

Figure 3 – Quadratic Bézier curve with points obtained for $m = 0.5$. P_0 and P_2 are the endpoints and P_1 is the control point of the curve.



Source: (SIMONI, 2005 - Adapted)

2.7.2 Bernstein's polynomials

Since Bézier curves are polynomials, they can be described in another polynomial basis of choice out convenience. Hence they can also be described using an explicit representation using Bernstein's polynomials (PRAUTZSCH; BOEHM; PALUSZNY, 2002; SIMONI, 2005).

A Bezier curve of degree "n" is given by equation (7):

$$\mathbf{B}^n(m) = \sum_{i=0}^n B_i^n(m) \mathbf{P}_i \quad (31)$$

where $B_i^n(m)$ represents the Bernstein's polynomials.

Equation (8) describes the Bernstein's polynomials:

$$B_i^n(m) = \binom{n}{i} m^i (1-m)^{n-i} \quad (32)$$

The binomial coefficients are given by equation (9):

$$\binom{n}{i} = \begin{cases} \frac{n!}{i!(n-i)!} & \text{if } 0 \leq i \leq n \\ 0 & \text{if } 0 > i > n \end{cases} \quad (33)$$

By the Bernstein's polynomials definition, it is possible to represent a Quadratic Bézier curve, as in equations (10) and (11):

$$\mathbf{B}^2(m) = \sum_{i=0}^2 B_i^2(m) \mathbf{P}_i \quad (34)$$

$$\mathbf{B}^2(m) = (1 - m)^2 \mathbf{P}_0 + 2m(1 - m) \mathbf{P}_1 + m^2 \mathbf{P}_2 \quad (35)$$

Bernstein's polynomial curve modeling is widely used in geometric parameterization problems for optimization because of their orthogonality properties, making the parametric sensitivities calculations well-conditioned. (CHIEREGATTI, 2019; KULFAN; BUSSOLETTI, 2006)

2.8 Optimization and Nelder-Mead method

An optimization problem, in general, consists of three main factors: the control variables, the objective function and constraints. The purpose of optimization problem is finding the value of the control variables that maximizes or minimizes the objective function. The variables are subject to a set of constraints that limit the values they can assume.

To solve complex engineering optimization problems, there are several algorithms and solvers suitable for different types of problems. The optimization algorithm used in this work is Nelder-Mead method (NELDER; MEAD, 1965), one of the most popular derivative-free methods, which is a COMSOL default.

The derivative-free solvers are characterized by not needing to compute derivatives of the objective function with respect to the control variables. They are of great importance nowadays due to the growing need to solve optimization problems defined by functions for which derivatives are unavailable or available at a prohibitive cost (CONN; SCHEINBERG; VICENTE, 2009). Derivative-free methods are suitable for problems where the objective function contains noise. Optimization problems whose control variables define geometry dimensions, such as the cases in this study, are an example (COMSOL MULTIPHYSICS, 2018).

The Nelder-Mead solver has been extensively used in engineering problems because of its simplicity and its ability to adapt to the curvature of the function being minimized (CONN; SCHEINBERG; VICENTE, 2009). This method seeks to improve

the worst point in the simplex performing a reflection, an expansion or a contraction (COMSOL MULTIPHYSICS, 2018).

The algorithm evaluates the objective function at a finite number of points per iteration and decides which action to take next solely based on those function values and without any explicit or implicit derivative approximation or model building (CONN; SCHEINBERG; VICENTE, 2009). Nelder and Mead (1965) describe the method for the minimization of a function of N variables, which depends on the comparison of function values at the $(N + 1)$ vertices of a general simplex, followed by the replacement of the vertex with the highest value by another point.

The Nelder-Mead algorithm employing a parallelization strategy is used in this work. The optimization solver is implemented in COMSOL Multiphysics (COMSOL MULTIPHYSICS, 2018), with a parallel version described by Lee and Wiswall (2007). The algorithm seeks to solve the problem $\min_{\theta \in \Phi} f(\theta)$, where θ is a N dimensional vector:

The algorithm follows 4 steps, considering P the degree of parallelization:

Step 1 - Create the initial simplex: an initial simplex with $N + 1$ points is created, A_0, A_1, \dots, A_N . The objective function at each point is evaluate and order the simplex points from best to worst: $f(A_0) < f(A_1) < \dots < f(A_N)$.

Step 2 – Assign each processor one of the P worst points: it is assumed that the number of parameters is at least as great as the degree of parallelization ($N \geq P$). The parallel algorithm reflects the P worst points ($A_{N-P+1}, A_{N-P+2}, \dots, A_N$) through the centroid M of the remaining points (A_0, A_1, \dots, A_{N-P}), defined as

$$M = \frac{1}{N} \sum_{n=0}^{N-P} A_n \quad (36)$$

Each processor is assigned one of the P worst points, denoted A_n for $n = N - P + 1, N - P + 2, \dots, N$, and calculates the reflection point for their assigned point as

$$A_n^R = M + \alpha(M - A_n) \quad (37)$$

where $\alpha > 0$ is an algorithm parameter, typically $\alpha = 1$.

Step 3 – Each processor returns and updated point: each of the processor evaluates the objective function at their reflection point A_n^R . A_n^* is the point that each processor

returns and it is from the set $\{A_n, A_n^R, A_n^E, A_n^C\}$, where A_n is one of the worst P points on the original simplex, A_n^R is the reflection, A_n^E the expansion and A_n^C the contraction point. The specific set of instructions for each processor are as follows:

Case 1: If the calculated reflection point A_n^R is an improvement over the initial best point A_0 , then we continue to move in the same direction by calculating the expansion point A_n^E . If A_n^E is an improvement over A_0 , then the processor returns the expansion point $A_n^* = A_n^E$. If A_n^E is not an improvement over A_0 , then the processor returns the reflection point $A_n^* = A_n^R$.

$$A_n^E = A_n^R + \gamma(A_n^R - M) \quad (38)$$

where $\gamma > 0$ is an algorithm parameter, typically $\gamma = 1$.

Case 2: If A_n^R is not an improvement over A_0 , but A_n^R is better than the next worst point A_{n-1} , then the processor returns $A_n^* = A_n^R$.

Case 3: If A_n^R is worse than the next worst point A_{n-1} , then the processor calculates the contraction point A_n^C as

$$A_n^C = \beta(M + \tilde{A}_n) \quad (39)$$

where:

$0 < \beta < 1$ is an algorithm parameter, typically $\beta = 1/2$

$\tilde{A}_n = A_n^R$ if $f(A_n^R) < f(A_n)$ and $\tilde{A}_n = A_n$ otherwise.

If A_n^C is an improvement over \tilde{A}_n , then the processor returns the contraction point $A_n^* = A_n^C$. If the contraction point is not an improvement, then the processor returns $A_n^* = \tilde{A}_n$, which is either A_n^R or A_n .

Step 4 – Form the new simplex: The P processors return P points, all of which could be new points as determined above. If for any processor, Case 1 or 2 apply or if Case 3 applies and $A_n^* = A_n^C$, then the new $N + 1$ dimension simplex is:

$$[A_0, A_1, \dots, A_{N-P}, A_{N-P+1}^*, A_{N-P+2}^*, \dots, A_N^*] \quad (40)$$

If Case 1, Case 2, or Case 3 and $A_n^* = A_n^C$ do not apply to any of the processors, then the entire simplex shrinks toward the best point A_0 . The new simplex is defined by these $N + 1$ points:

$$[A_0, (\tau A_0 + (1 - \tau)A_1), (\tau A_0 + (1 - \tau)A_2), \dots, (\tau A_0 + (1 - \tau)\tilde{A}_{N-p+1}), (\tau A_0 + (1 - \tau)\tilde{A}_{N-p+2}), \dots, (\tau A_0 + (1 - \tau)\tilde{A}_N)] \quad (41)$$

where $0 < \tau < 1$ is an algorithm parameter, typically $\tau = 1/2$.

After the new simplex is formed, the points are reordered by their objective function values and return to Step 2.

3 METHODOLOGY

The present work aimed to develop optimization of a liquid-liquid ejector's geometry to maximize the efficiency of the device. To perform this optimization, the ejector boundaries were constructed using parameterized curves. Such curves were quadratic Bézier curves, with parameterized control points. Computational fluid dynamics (CFD) simulations combined to the Nelder–Mead optimization technique were performed to optimize the parameters of the Bézier curves. The commercial software COMSOL Multiphysics, whose license is available through the FAPESP-RCGI project (FAPESP Proc. 2014/50279-4), was used to perform numerical modeling, simulations, and parametric optimization of the ejector.

3.1 Ejector geometry definition

The ejector geometry shown in Figure 4 was built as the base for the initial simulations and optimizations. This geometry was constructed on COMSOL with dimensions similar to those used by (SANGER, 1968a). In this base geometry, only the curves that limit the suction chamber, primary inlet and nozzle are quadratic Bézier curves. The rest of the boundaries are made up of straight lines.

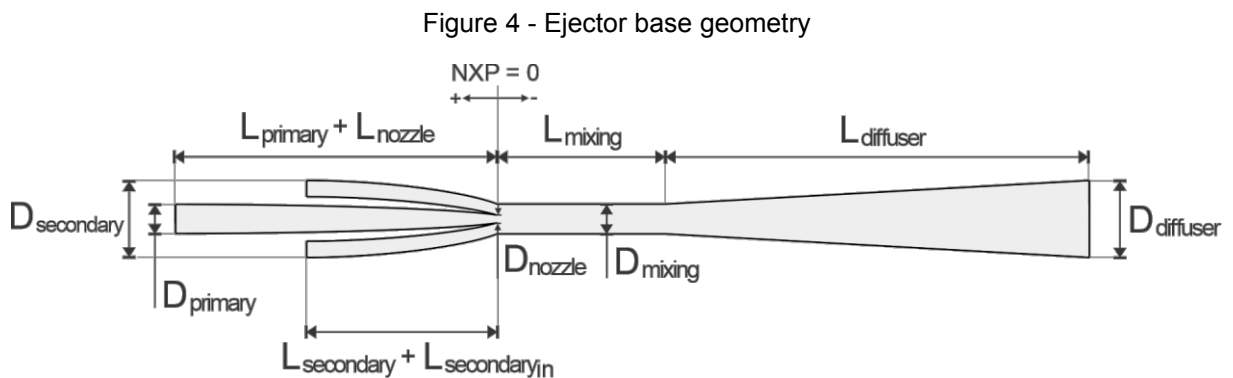


Table 1 shows the values, in millimeters, of the geometric parameters used in the ejector construction and their respective symbols.

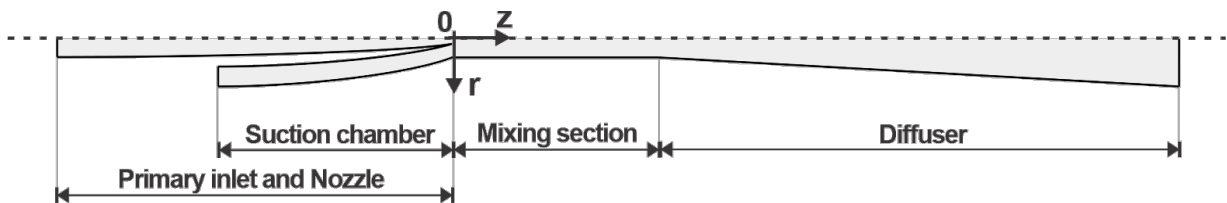
Table 1 - Geometric parameters for ejector construction

Geometric parameter	Value [unit]	Symbol
Diameter of the nozzle	8.81 [mm]	D_{nozzle}
Diameter of the secondary inlet	88.5 [mm]	$D_{secondary}$
Diameter of the primary inlet	33.5 [mm]	$D_{primary}$

Geometric parameter	Value [unit]	Symbol
Diameter of the diffuser	88.5 [mm]	$D_{diffuser}$
Diameter of the mixing chamber (throat)	34.2 [mm]	D_{mixing}
Length of the mixing chamber	194 [mm]	L_{mixing}
Length of the diffuser	490 [mm]	$L_{diffuser}$
NXP - distance between nozzle outlet and mixing chamber inlet	0 [mm]	NXP
Length of the convergent section of the nozzle	71.4 [mm]	L_{nozzle}
Length of the primary nozzle inlet	300 [mm]	$L_{primary}$
Length of the secondary	70 [mm]	$L_{secondary}$
Length of the secondary inlet	150 [mm]	$L_{secondary_{in}}$
Maximum thickness of the nozzle's walls	8.85 [mm]	$thickness$

To perform the optimizations, the axisymmetric geometry of the ejector was used, as shown in Figure 5. The use of axisymmetric geometry makes it possible to decrease the computational effort, and even improve the mesh refinement to improve the quality of results. Figure 5 also shows the basic components of the ejector and the origin of the radial (r) and axial (z) axes.

Figure 5 – Axisymmetric ejector geometry



Quadratic Bézier curves constitute the suction chamber, primary inlet and nozzle boundaries. Table 2 shows the coordinates of the control point of each curve. In Figure 6, each of the three curves are identified. For some cases considered in this study (cases 6, 7 and 8), the curve that constitutes the diffuser boundary was also parameterized as a quadratic Bézier curve, as shown in Figure 7. The coordinates of the control point of curve 4 are also shown in the Table 2.

Table 2 – Coordinates of the control points

Bézier curve	Control point	Coordinates of the control point (r, z)
Curve 1	$P_{1(I)}$	$\left(\frac{D_{secondary}}{2}, -L_{secondary}\right)$
Curve 2	$P_{1(II)}$	$\left(\frac{D_{primary}}{2} + thickness, -L_{secondary}\right)$
Curve 3	$P_{1(III)}$	$\left(\frac{D_{primary}}{2}, -L_{nozzle}\right)$
Curve 4	$P_{1(IV)}$	$\left(\frac{D_{mixing}}{2}, L_{mixing} + \frac{L_{diffuser}}{3}\right)$

Figure 6 - Quadratic Bézier in primary inlet, nozzle, and secondary inlet

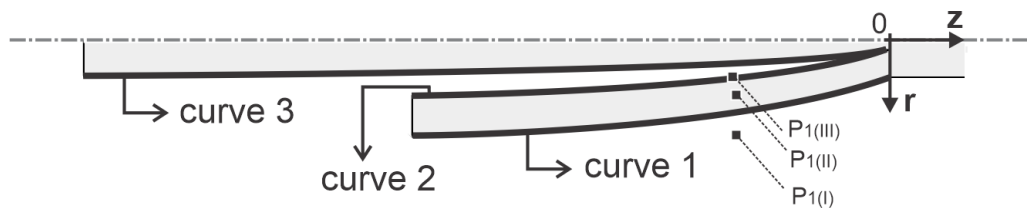
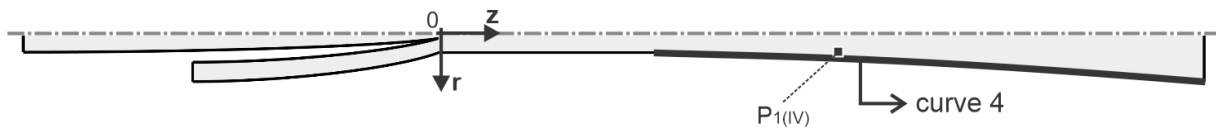


Figure 7 - Quadratic Bézier in diffuser (cases 6, 7 and 8)



3.2 Computational set-up

This work used CFD simulations performed in the commercial software COMSOL (version 5.3a and 5.5). COMSOL employs a finite element discretization scheme. Navier-Stokes and the turbulence transport equations are solved using a segregated approach. Two or three iterations are performed for the turbulence transport equations for each iteration in the Navier-Stokes group. The iterative solver for the turbulence transport equations is a damped Newton method with constant damping factor.

The following assumptions were considered in computer simulations:

- i. Two-dimensional axisymmetric;
- ii. Incompressible flow;
- iii. Steady-state flow;
- iv. Newtonian fluid;
- v. Constant viscosity;

- vi. Adiabatic;
- vii. Primary and secondary fluids are water at 26.7°C.

The turbulence model used was k- ω SST (MENTER; KUNTZ; LANGTRY, 2003) with *automatic wall treatment* selected as wall function. The automatic wall treatment gives a robust formulation that makes the most out of the available resolution because switches between a low-Reynolds-number formulation and a wall function formulation depending on how well resolved the flow is close to the wall (COMSOL, 2017). The modelled ejector operates in a Reynolds range based on the mixing chamber mean velocity and diameter that varies between 153,252 (for $M = 1.0$) and 612,991 (for $M = 7.0$). The turbulence model k- ω SST is suitable to capture the LJI ejector flow characteristics (MARUM et al., 2021). k- ω SST was applied with “Stationary with initialization” study on COMSOL. The step 1, wall distance initialization, considered a relative tolerance of 10^{-6} and the step 2, stationary, considered 0.001 as relative tolerance for all quantities.

Table 3 showed the boundary conditions used for setting up the computational simulations. k is the turbulent kinetic energy, ω is the turbulent dissipation rate, U_{ref} is the normal velocity, L_t is the turbulence length scale (equal to $0.07 \cdot L$), L is the diameter of the fluid inlets, I_t is the turbulent intensity (equal to 0.05) and G is reciprocal wall distance.

Table 3 - Boundary conditions

Boundary	Flow Condition	Turbulence condition
Walls	No slip	automatic wall treatment
Primary inlet	Normal velocity equals to 2.0 m/s ($Q_1 = 1.77 \cdot 10^{-3} \text{ m}^3/\text{s}$)	$k = \frac{3}{2} (U_{ref} I_t)^2$ $\omega = \frac{1}{k^{\frac{1}{2}} (\beta_0^*)^{\frac{1}{4}} L_T}$
Secondary inlet	Normal velocity (varies with M)	$\nabla G \cdot \mathbf{n} = 0$
Diffuser outlet	$2.06 \cdot 10^5 \text{ Pa}$	$\nabla k \cdot \mathbf{n} = 0$ $\nabla \omega \cdot \mathbf{n} = 0$ $\nabla G \cdot \mathbf{n} = 0$

3.3 Optimization set-up

The optimization performed in this work was done by using Optimization Study on COMSOL. The optimization algorithm used was the Nelder-Mead method, which has been described in section 2.8. The Nelder-Mead method was applied with optimality tolerance of 0.01 and maximum number of model evaluations equal to 1000.

3.3.1 Control variables and parameters

Initially, six control variables were considered for the proposed optimization problem. These variables correspond to parameters that are multiplied to the coordinates of the control points of the Bézier curves. Then, two more parameters were also considered for the optimization of the nozzle (NXP and diameter). With the parameterization of the diffuser curve, four other parameters were included. To analyze the effect of the optimization of the inlet diameters, two new parameters are added.

The fourteen total optimization parameters (control variables) are shown in Table 4. Parameters p_1 to p_7 and p_9 to p_{14} are multiplied by certain coordinates of ejector points. Their initial value is 1, because initially they do not change the point. Parameter p_8 is added to the NXP coordinate value, so its initial value is 0.

Table 4 - Optimization parameters and description

Optimization parameter	Description	Initial value
p_1	Multiplied by the r coordinate of curve 1 control point - $P_{1(I)}$	1
p_2	Multiplied by the z coordinate of curve 1 control point - $P_{1(I)}$	1
p_3	Multiplied by the r coordinate of curve 2 control point - $P_{1(II)}$	1
p_4	Multiplied by the z coordinate of curve 2 control point - $P_{1(II)}$	1
p_5	Multiplied by the r coordinate of curve 3 control point - $P_{1(III)}$	1
p_6	Multiplied by the z coordinate of curve 3 control point - $P_{1(III)}$	1
p_7	Multiplied by the nozzle diameter	1
p_8	Increment to NXP	0
p_9	Multiplied by the diffuser diameter	1
p_{10}	Multiplied by the mixing chamber length	1
p_{11}	Multiplied by the r coordinate of curve 4 control point - $P_{1(IV)}$	1

Optimization parameter	Description	Initial value
p_{12}	Multiplied by the z coordinate of curve 4 control point - $P_{1(IV)}$	1
p_{13}	Multiplied by $D_{secondary}$ in the geometry construction	1
p_{14}	Multiplied by $D_{primary}$ in the geometry construction	1

3.3.2 Objective function

The ejector efficiency equation is the objective function to be maximized of the optimization problems of this work.

The efficiency equation for an incompressible fluid ejector can be written as equation (42) (WINOTO; LI; SHAH, 2000).

$$\eta = M \cdot N \quad (42)$$

$$N = \frac{P_d - P_s}{P_i - P_d} \quad (43)$$

where:

M – entrainment ratio (the ratio between volumetric flow ratio of the secondary fluid Q_2 and volumetric flow ratio of the primary fluid Q_1);

N – pressure ratio;

P_d – total pressure at the diffuser outlet;

P_s – total pressure at the suction chamber inlet;

P_i – total pressure at the primary inlet.

An interpretation of this equation is how much power the secondary fluid receives ($\rho \cdot Q_2 \cdot (P_d - P_s)$) in relation to the amount of power spent by the primary ($\rho \cdot Q_1 \cdot (P_i - P_d)$).

3.3.3 Constraints

The problem constraints are the lower and upper bounds that the optimization parameters can assume. Table 5 shows the bounds for each parameter. From the optimization point of view, the constraints improve the convergence of the method. The choice of these bounds is satisfactory, since the parameters did not reach the limits

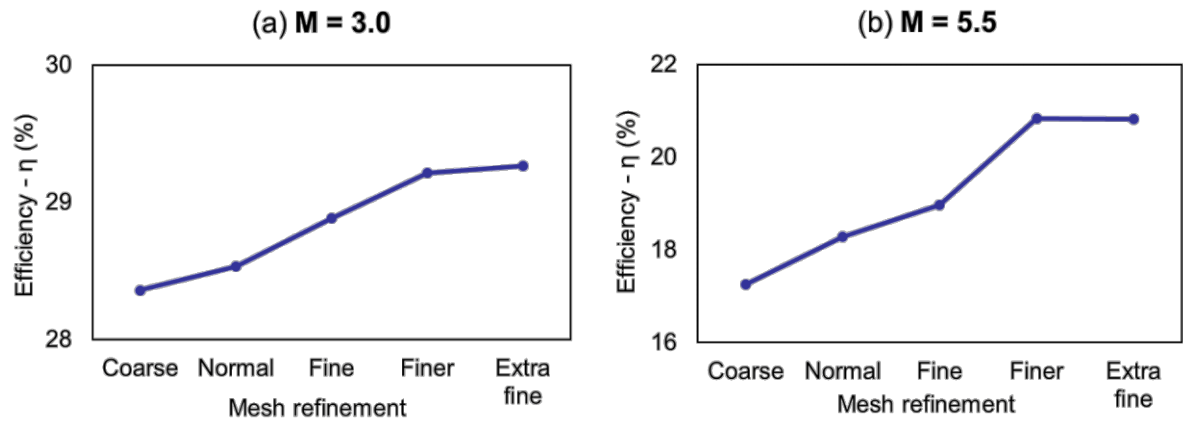
imposed after the optimization (with the exception of the parameter p_8 , but the increase in their limit did not lead to significant changes in the value of the objective function).

Table 5 - Lower and upper bounds of optimization parameters. Every parameter is nondimensional except p_8 .

Optimization parameter	Lower bound	Upper bound
p_1	0.5	3.0
p_2	0.5	3.0
p_3	0.5	3.0
p_4	0.5	3.0
p_5	0.5	3.0
p_6	0.5	3.0
p_7	0.5	1.5
p_8	-0.02 [m]	0.02 [m]
p_9	0.5	2.0
p_{10}	0.5	2.0
p_{11}	0.8	1.5
p_{12}	0.5	1.5
p_{13}	0.5	2.0
p_{14}	0.5	2.0

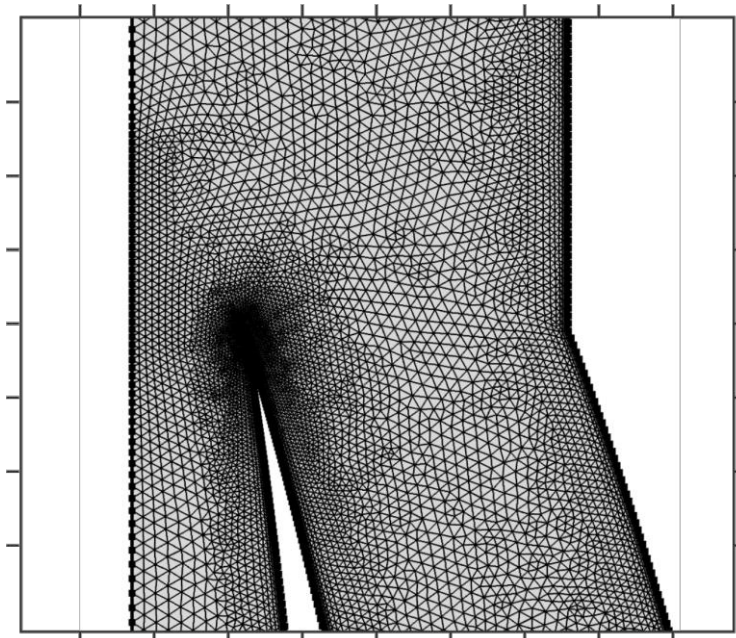
3.4 Mesh convergence

Five different mesh sizes were tested to assess convergence. The ejector efficiency results, for $M = 3.0$ and $M = 5.5$, are shown in Figure 8 as a function of the mesh size. The evaluated meshes were: Coarse (29492 elements), Normal (44480 elements), Fine (101898 elements), Finer (335606 elements) and Extra finer (813142 elements).

Figure 8 - Mesh convergence for $M = 3.0$ (a) and $M = 5.5$ (b)

In both cases, convergence was achieved from the mesh with *finer element size* of COMSOL, which was the mesh used in the other simulations of this study. Complete mesh consists of 328439 domain elements and 7167 boundary elements. The mesh is composed of triangular elements and it presents quadrilateral elements in the boundary layer. Mesh details at the inlet of the mixing chamber are shown in the Figure 9.

Figure 9 - Mesh details at the mixing chamber inlet

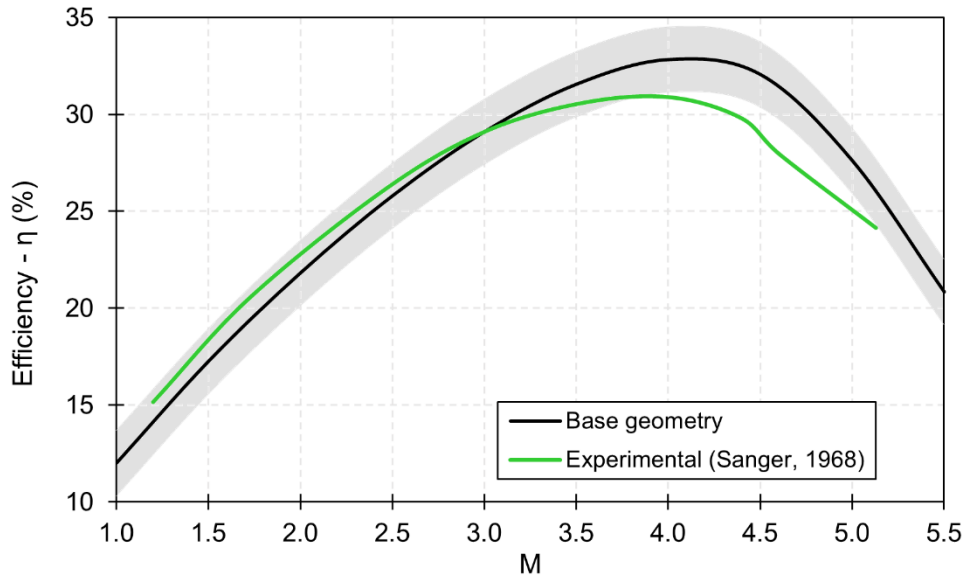


3.5 Validation of the simulations

As previously described, the ejector base geometry was constructed on with dimensions similar to those used in experimental studies by Sanger (1968a). In Sanger (1968a), the performance of liquid-liquid ejector was evaluated experimentally and flow profiles from selected sections were provided.

Figure 10 presents the efficiency curve obtained with simulation data of the base geometry compared to the experimental curve. For M values greater than 3.0, the simulated data for the base geometry overestimated the efficiency values and the peak efficiency of the two curves does not occur at the same value of entrainment ratio (M). These deviations occur due to the small differences between the geometries and probably by the diffusive region in the diffuser (see Figure 23 about energy dissipation rate field). Despite this difference, the simulation predicted satisfactorily the peak position of the ejector's efficiency, at a value of M close to the experimental one, in addition to maintaining the shape of the efficiency curve. It is then considered that the simulated data curve had a fair fit with the experimental curve (RMSE = 1.687), considering the simplifications adopted in the geometry and computational model. The RMSE was calculated by the difference between the experimental values and the values of the base geometry obtained for the same M . Figure 10 also shows an uncertainty range (in gray), corresponding to the efficiency values of the base geometry \pm RMSE. Considering this range of CFD uncertainty and the experimental uncertainty (which is unknown), the ranges overlap, which reinforces that the validation is satisfactory.

Figure 10 - Efficiency curve for simulated base geometry compared to the experimental curve - $M = Q_2/Q_1$. The gray area represents the range $\pm 1 \cdot RMSE$



The total pressure profiles were plotted in two positions in the mixing chamber and in one position in the diffuser for $M = 3.75$, value of entrainment ratio for which Sanger (1968a) evaluated the pressure profiles. These positions, along the axial axis, correspond to x/D_{mixing} equals to 2.6, 4.8 and 10.4. The profiles were compared with experimental data from Sanger (1968a) and shown in the Figure 11.

Figure 11 - Simulated total pressure profiles compared to the profiles obtained by Sanger (1968a)

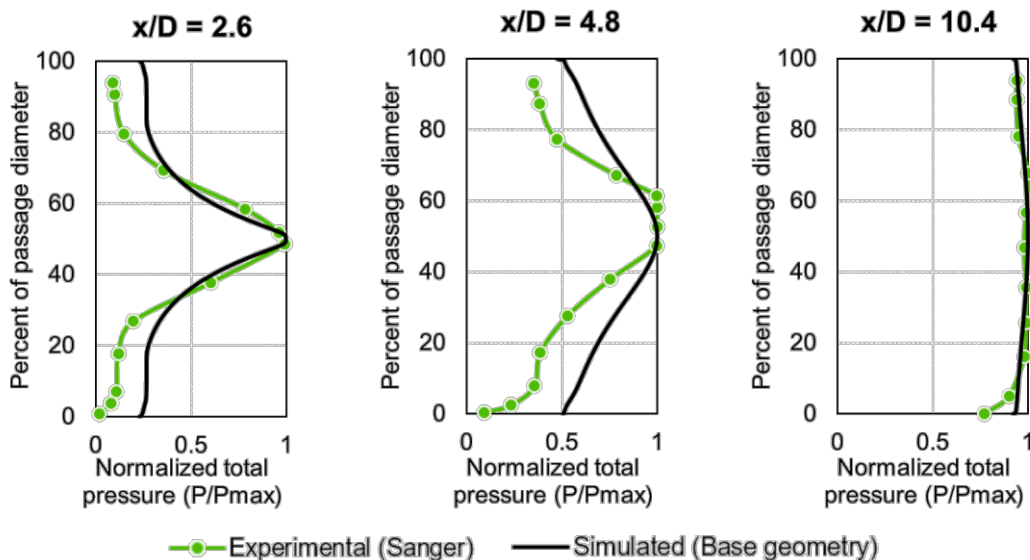


Figure 11 allows to compare the predicted the total pressure in different axial positions along the ejector with the experimental data and to identify why the performance curves are an imperfect match. It is shown that the simulated results are

in fair agreement with the experimental data, despite the pressure at positions close to the ejector wall being overestimated which are due to fine differences on lacking geometry description and on the wall treatment needed for computational simulations. The pressure profiles of the simulation results are more homogeneous than the experimental profiles, which may justify the overestimation of the efficiency observed in the Figure 10 for $M > 3.5$.

3.6 Evaluated cases

Ten cases of optimization of the presented ejector were evaluated. The cases were chosen to verify the influence of the components and parameters of the ejector and the operational condition (entrainment ratio - M) on its efficiency, as well as in the homogeneity of the flow fields. The first cases evaluated the influence of the fluid inlet regions. After that, the influence of the nozzle parameters (diameter and NXP) was verified. The effect of optimizing the length of the mixing chamber and diffuser and the diameter of the primary and secondary inlets was also analyzed. Finally, the effect of optimization for more than one operating condition at the same time (M value) was evaluated. The tested cases have the following characteristics:

- **Case 1:** optimization of control points for curves 1, 2 and 3, which delimit the suction chamber, the primary inlet, and the nozzle, for $M = 3.0$. In this case, the parameters from p_1 to p_6 are optimized.
- **Case 2:** optimization of control points for curves 1, 2 and 3, which delimit the suction chamber, the primary inlet, and the nozzle, for $M = 5.5$. In this case, the parameters from p_1 to p_6 are optimized.
- **Case 3:** case 2 with the inclusion of parameter p_7 , corresponding to the nozzle diameter.
- **Case 4:** case 2 with the inclusion of parameter p_8 , corresponding to the NXP.
- **Case 5:** case 2 with the inclusion of parameter p_7 and p_8 simultaneously.
- **Case 6:** parameterization of the curve that delimits the diffuser as a Bézier quadratic. This case is only to compare the influence of a curve at the diffuser boundary and, therefore, does not involve optimization.
- **Case 7:** optimization of the diffuser curve. The parameters p_1 to p_6 continue to be optimized, with the inclusion of p_9 (diffuser diameter), p_{10} (length of the

mixing chamber), p_{11} and p_{12} (coordinates of the control point of curve 4). The optimization was performed for $M = 5.5$.

- **Case 8:** this case involves the simultaneous optimization of parameters p_1 to p_{12} . It is like case 7, with the inclusion of parameters related to the nozzle diameter (p_7) and NXP (p_8).
- **Case 9:** optimization that includes parameters of the primary and secondary inlets diameters. This case optimizes the parameters from p_1 to p_6 and includes the parameters p_{13} and p_{14} , for $M = 5.5$. Its results are compared to those in case 2.
- **Case 10:** this case optimizes the parameters from p_1 to p_8 , as well as case 5, but for three values of M at the same time, having as objective function the sum of the efficiencies for each M .

4 RESULTS AND DISCUSSIONS

4.1 Influence of the entrainment ratio (M) used in the optimization

Cases 1 and 2 optimize the first six parameters (p_1 to p_6), which correspond to the control points of the Bézier curves of the inlets, for two different M values: 3 and 5.

The results of the optimization (parameters and objective function) for $M = 3$ are shown in Table 6. It is possible to observe a significant change in the parameters with the optimization, which consequently alters the control points of the Bézier curves. With the change in the curves, the objective function reached the optimized value of 0.366. Table 7 shows the results of the optimization for $M = 5.5$ (case 2). As in the case 1, it is possible to verify the increase in the value of the objective function because of the change in the optimization parameters, which modify the geometry. The objective function reached the optimized value of 0.2797. The optimized geometries for case 1 and case 2, compared to base case, can be seen in Figure 12.

Table 6 - Optimization results for $M=3.0$ (case 1)

$M = 3.0$							
Parameters						Objective function	
p_1	p_2	p_3	p_4	p_5	p_6	Initial	Optimized
0.99543	1.1183	0.6307	1.3229	1.037	1.3026	0.2911	0.3660

Table 7 - Optimization results for $M=5.5$ (case 2)

$M = 5.5$							
Parameters						Objective function	
p_1	p_2	p_3	p_4	p_5	p_6	Initial	Optimized
1.0995	1.1813	1.4623	0.57622	1.7006	0.51007	0.2084	0.2797

Figure 12 - Original geometry (a) compared to optimized geometry for case 1 (b) and 2 (c)

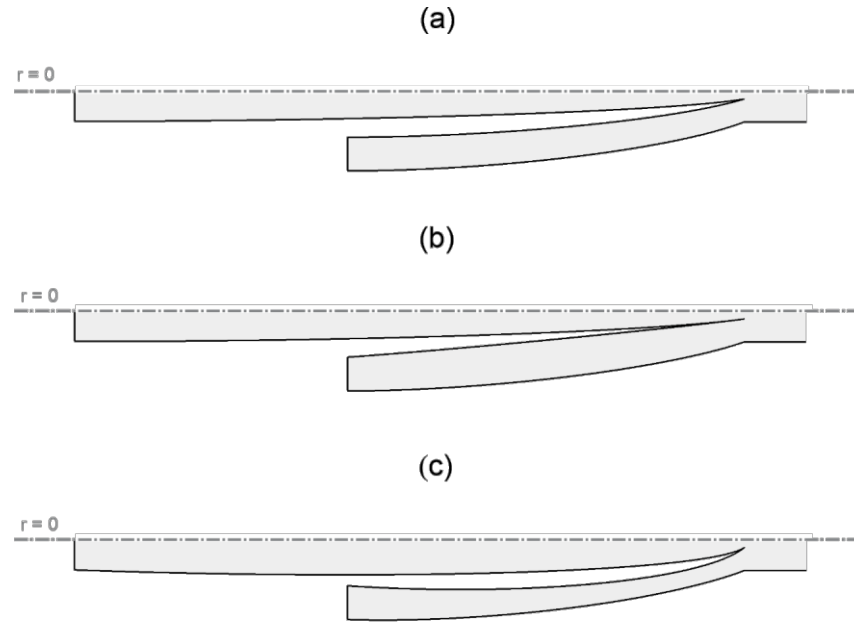
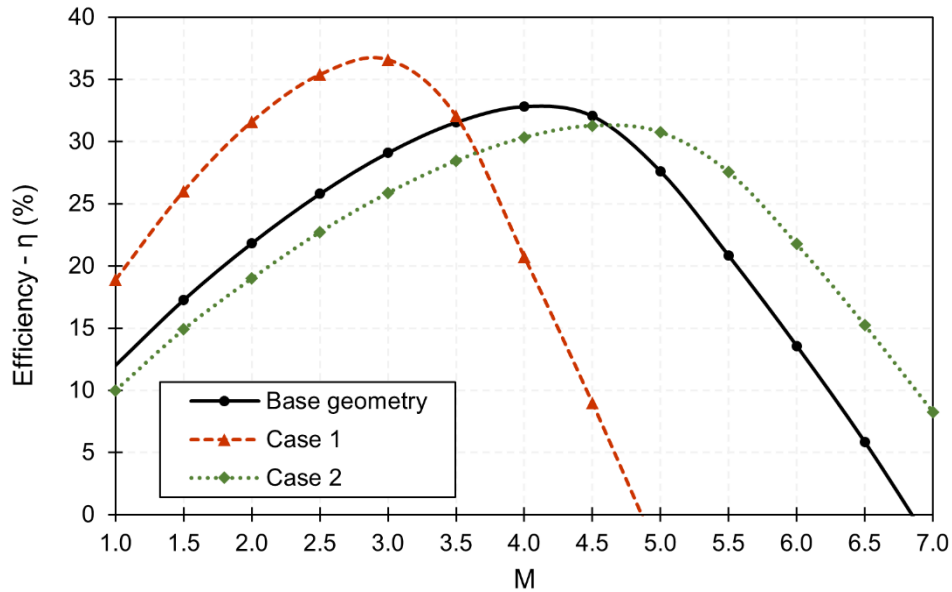


Figure 13 shows the efficiency curves for the geometries optimized for $M = 3$ and $M = 5.5$. For case 1, it is observed that the maximum efficiency value exceeded 35%, higher than the value around 33% of the base geometry. In addition, the most efficient operational condition has also changed from an entrainment ratio M between 4 and 4.5 to an entrainment ratio M close to 3. For case 2, the most efficient operational condition has changed to an entrainment ratio close to 5. However, the maximum efficiency value did not exceed the value for the original geometry.

Comparing the curves of Figure 13 it is observed that the efficiency curves optimized for higher M values present a smoother shape than the curves optimized for lower M values. For optimizations for $M = 3$, high efficiency values are more sensitive to changes in operating conditions. On the other hand, for optimizations for $M = 5.5$ the efficiency curve has a broader peak, the efficiency values remain close to the maximum value in a larger range of M .

Figure 13 - Ejector efficiency with geometry optimized for $M = 3.0$ and $M = 5.5$ as a function of the entrainment ratio compared to efficiency curve of the base geometry



Cases 3 to 8 used the operational condition of $M = 5.5$ in the optimizations. The less sensitive behavior to changes in efficiency with the M values and the peak of efficiency located at higher entrainment ratios (around $M = 5.0$) justify this choice. It is interesting that the ejector operates at higher M , thus at higher entrainment ratio of the secondary flow, and with a lower sensitivity of variation of efficiency to changes in flow rates.

4.2 Effect of nozzle and NXP optimization

In case 3, besides the control points of Bézier curves, the nozzle diameter was optimized. The results of optimization for this case were shown in Table 8. It can be seen from values of optimized parameter in table and the geometry in Figure 14 (b) that the parameter p_7 changed the geometry by reducing the nozzle diameter about 87% of the original value (original value = 8.81 mm, optimized value = 7.66 mm). The optimized efficiency for this case reached 0.312, greater than that of case 2, which does not consider the nozzle diameter.

Table 8 - Optimization results for $M=5.5$ with nozzle diameter optimized (case 3)

$M = 5.5$								
Parameters							Objective function	
p_1	p_2	p_3	p_4	p_5	p_6	p_7	Initial	Optimized
1.1405	1.2278	1.1072	1.2297	1.0663	1.3606	0.87072	0.2084	0.31165

The optimized parameter values for case 4 indicate a moving the nozzle outlet away from the mixing chamber inlet ($NXP = 0.02\text{ m}$), confirm it can be seen in Table 9 and in Figure 14 (c). The objective function for this case was even greater than that of case 3, which considers the optimization of the nozzle diameter reaching a value of 0.323.

Table 9 - Optimization results for $M=5.5$ with NXP optimized (case 4)

$M = 5.5$									
Parameters								Objective function	
p_1	p_2	p_3	p_4	p_5	p_6	p_8	Initial	Optimized	
1.1735	1.4788	1.3124	0.65105	1.6713	0.76263	-0.02	0.2084	0.32333	

The optimization performed in case 5 resulted in a composition of the results seen in cases 3 and 4. The optimized parameters in Table 10 and the geometry optimized in Figure 14 (d) show a reduction in the nozzle diameter (parameter p_7) about 92% of the initial value (original value = 8.81 mm, optimized value = 8.11 mm). In addition, the nozzle moved away from the suction chamber (parameter p_8), as in case 4.

Table 10 - Optimization results for $M=5.5$ with nozzle diameter and NXP optimized (case 5)

$M = 5.5$									
Parameters								Objective function	
p_1	p_2	p_3	p_4	p_5	p_6	p_7	p_8	Initial	Optimized
1.1193	1.2503	0.5282	1.2475	0.8412	1.2235	0.9155	-0.02	0.2084	0.33176

Figure 14 - Base geometry (a) compared to optimized geometries for $M = 5.5$: (b) case 3, (c) case 4 and (d) case 5

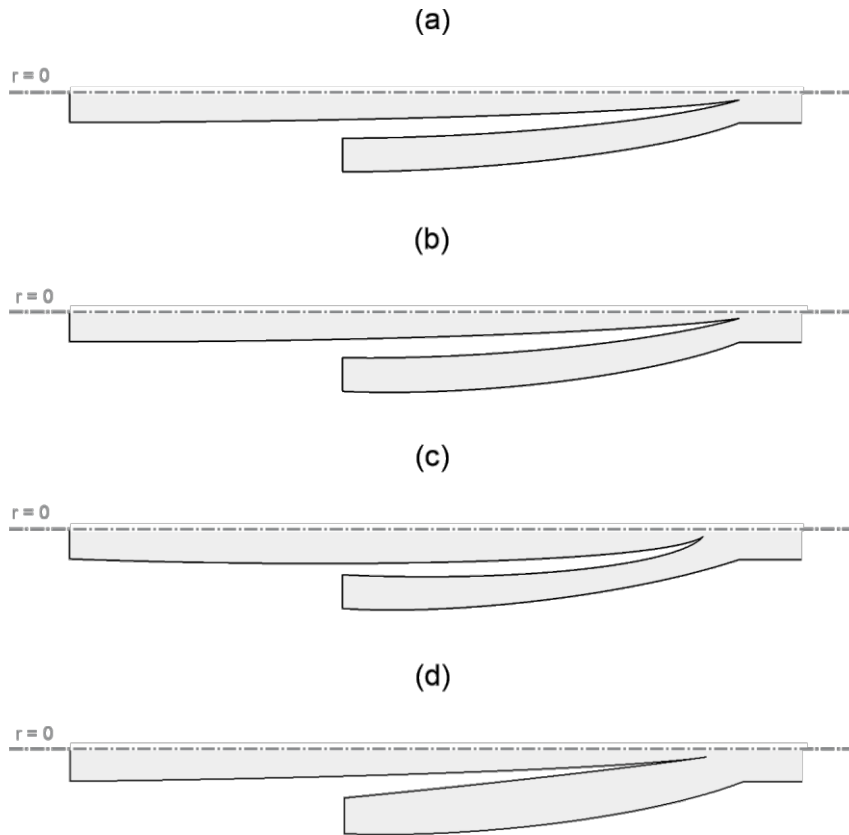
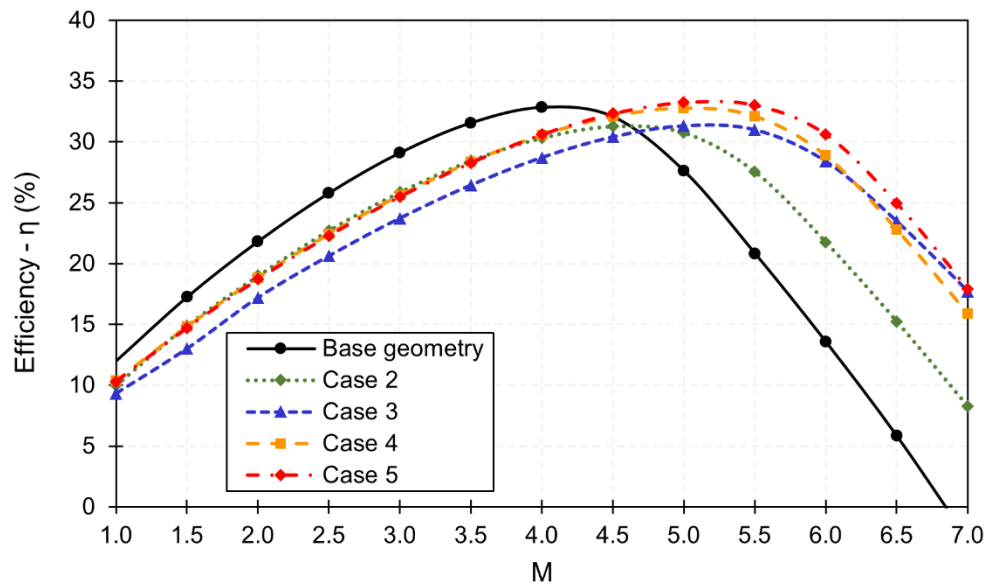


Figure 15 shows the efficiency curve as a function of M for case 2, 3, 4 and 5. Comparing the curves with those for the base geometry and for the optimization that does not consider nozzle diameter and NXP, there is a greater displacement in the efficiency curve and an increase in the maximum efficiency value. Simulations that considered the nozzle diameter and the nozzle position along ejector axis (NXP) as parameters of the optimization process resulted in higher efficiency values than those that kept these parameters fixed for $M > 4.5$. With these results, it is noticeable that the nozzle diameter and the NXP exert a great influence on the efficiency curve of the ejector.

Figure 15 - Ejector efficiency with geometry optimized for $M = 5.5$ as a function of the entrainment ratio

4.3 Effect of parameterization and optimization of the diffuser boundary

Case 6 considered the diffuser boundary as a quadratic Bézier curve, as seen in Figure 16 (a). No optimizations were made, only the parameterization of the new curve is considered. A considerable increase in the efficiency of the ejector was observed, as can be seen from the Table 11, for $M = 5.5$.

Table 11 - Value of parameters and efficiency for case 6

$M = 5.5$						Objective function
Parameters						
p_1	p_2	p_3	p_4	p_5	p_6	Initial 0.3086
1	1	1	1	1	1	
p_7	p_8	p_9	p_{10}	p_{11}	p_{12}	
1	0	1	1	1	1	

The optimization including the diffuser curve resulted in the optimized parameters presented in the Table 12 for case 7. Figure 16 (b) represents the optimized geometry. It was found that the parameter related to the diffuser diameter (p_9) reduced to 67% of the original value, while the parameter related to the mixing chamber length increased by 24% from its initial value. There is also a change in the control points of the curves (parameters p_{11} and p_{12}), whose initial value was 1.

Table 12 - Optimization results for M=5.5 with diffuser curve optimized (case 7). p_7 and p_8 are not optimized here

$M = 5.5$						
Parameters						Objective function
p_1	p_2	p_3	p_4	p_5	p_6	Optimized
1.0999	1.0709	1.0523	1.0702	1.2470	0.80332	0.34851
p_7	p_8	p_9	p_{10}	p_{11}	p_{12}	
1	0	0.66826	1.2439	1.0492	0.96518	

Case 8 includes the optimization of all 12 parameters simultaneously. Table 13 shows the change in the parameters related to the control points of the Bézier curves (p_1 to p_6 , p_{11} and p_{12}). In addition, it is noted the separation of the nozzle from the mixing chamber (in the limit value allowed for the parameter, as well as in the other cases in which the parameter p_8 was considered), the reduction of the diffuser diameter to 80% of the original value and an increase 9% in the length of the mixing chamber, as seen in Figure 16 (c).

Table 13 - Optimization results for M=5.5 with diffuser curve, nozzle diameter and NXP optimized

$M = 5.5$						
Parameters						Objective function
p_1	p_2	p_3	p_4	p_5	p_6	Optimized
1.0299	1.0592	0.93453	1.1532	1.0067	1.0778	0.34964
p_7	p_8	p_9	p_{10}	p_{11}	p_{12}	
0.99314	-0.02	0.80755	1.088	1.0956	1.0455	

Figure 16 - Comparison of the geometries of case 6 (a), case 7 (b) and case 8 (c)

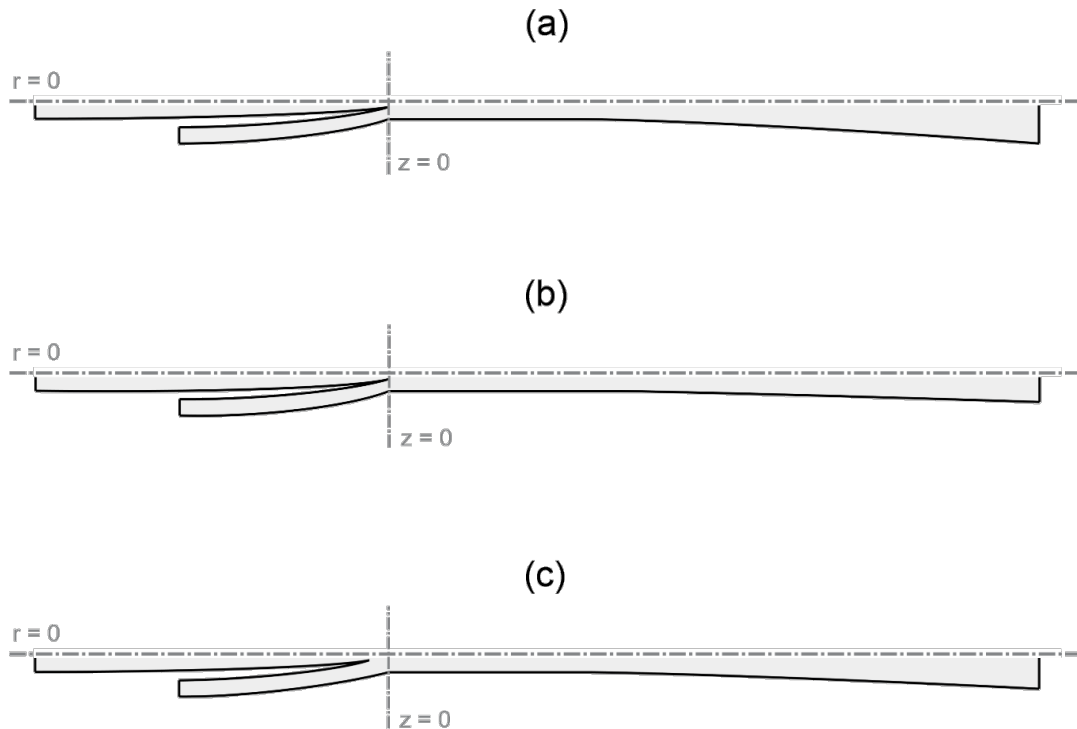
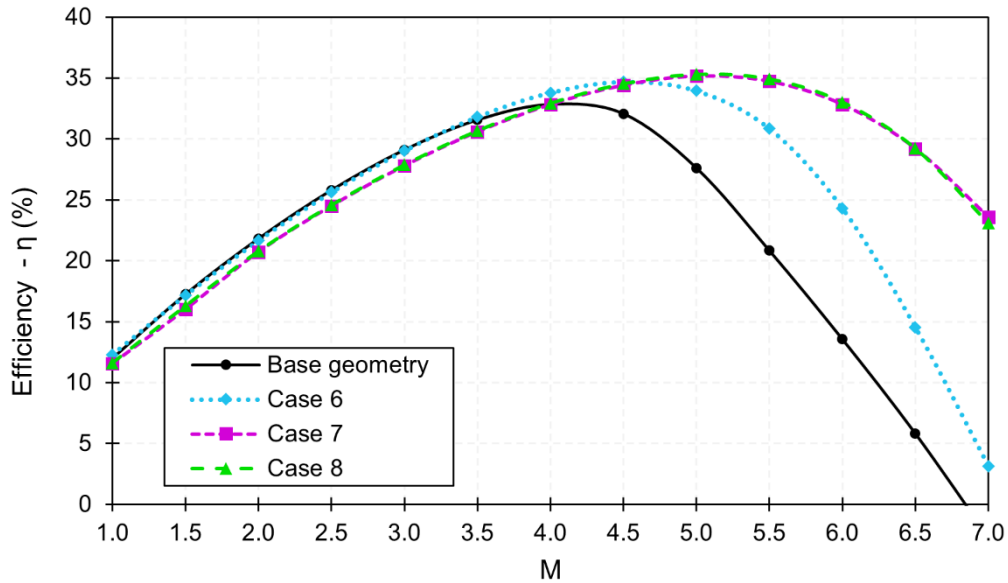


Figure 17 shows the efficiency curves for case 6, case 7 and case 8. For case 6, the curve indicates an improvement in the efficiency of the ejector from $M = 3.5$, only with the parameterization of the diffuser curve, without optimizations. The efficiency curve for case 7 demonstrates that for entrainment ratio above 4.0 the efficiency values are all greater than those in the base case and above $M = 4.5$ greater than in case 6.

Figure 17 shows that the efficiency curves for cases 7 and 8 are practically the same. These curves have a peak efficiency greater than 0.35 between $M = 5.0$ and $M = 5.5$. In addition, the curves are less sensitive to changes in the operating condition (in this case, entrainment ratio), compared to case 6 and base case. This effect demonstrates that the increase in the mixing region, either by moving away from the nozzle outlet or by increasing the length of the mixing chamber, is favorable for an improvement in the efficiency of the ejector. This is because there is a greater mixture between the primary and secondary fluids, favored by the increase in the mixing region.

Figure 17 - Ejector efficiency with geometry optimized for $M = 5.5$ as a function of the entrainment ratio (with parametrized diffuser curve)



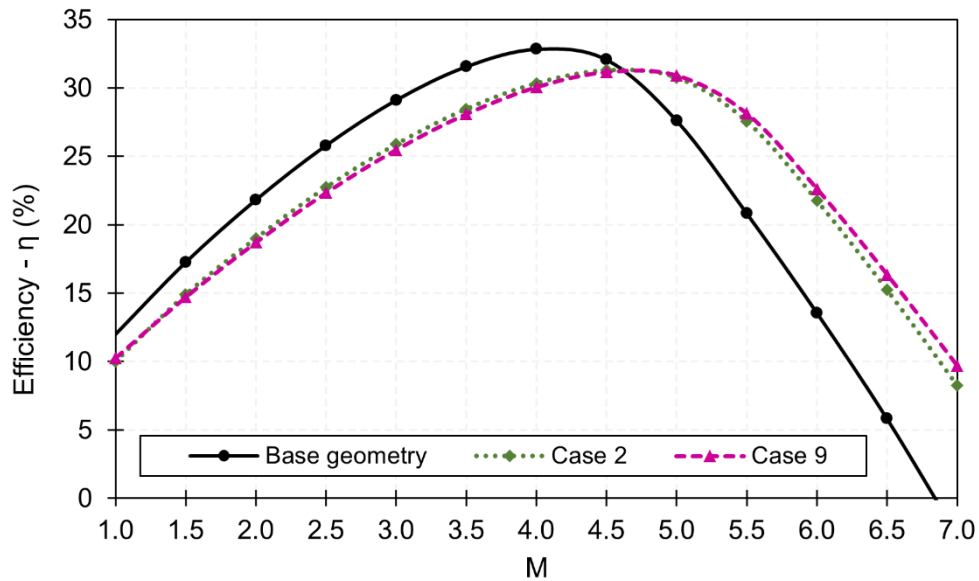
4.4 Effect of inlet diameters optimization

The results of the parameter values after the optimization of case 9 are shown in Table 14. It is observed that the parameters added in this case (p_{13} and p_{14}) changed by approximately 23% and 37%, respectively, increasing the diameters of fluid primary and secondary inlets in the ejector. However, when analyzing Figure 18, it is noted that this change in parameters did not generate significant changes in the efficiency curve, when compared with the optimization of case 2, which involves only the parameters p_1 to p_6 . Therefore, in the case analyzed, there was no influence of the diameter of the primary and secondary inlets on the efficiency curve of the ejector, on the displacement of the curve, value and position of the efficiency peak.

Table 14 - Optimization result for case 9

$M = 5.5$									
Parameters								Objective function	
p_1	p_2	p_3	p_4	p_5	p_6	p_{13}	p_{14}	Initial	Optimized
0.99373	1.1105	1.337	0.70851	1.4363	0.52672	1.2256	1.3659	0.2084	0.2833

Figure 18 - Ejector efficiency for base case, case 2 and case 9 as a function of the entrainment ratio



4.5 Effect of optimization for simultaneous M values

Table 15 shows the results of the parameters values and the objective function for the optimization performed in case 10. Three values of operational condition ($M = Q_2/Q_1$) were analyzed simultaneously, with the objective function being the sum of the efficiencies for $M = 2$, $M = 4$ and $M = 6$ (case 10 a) and $M = 3.5$, $M = 4.5$ and $M = 5.5$ (case 10 b), according to Equation (44) for case 10a. The same parameters as in case 5 have been optimized.

$$\text{Objective function} = \eta(M = 2) + \eta(M = 4) + \eta(M = 6) \quad (44)$$

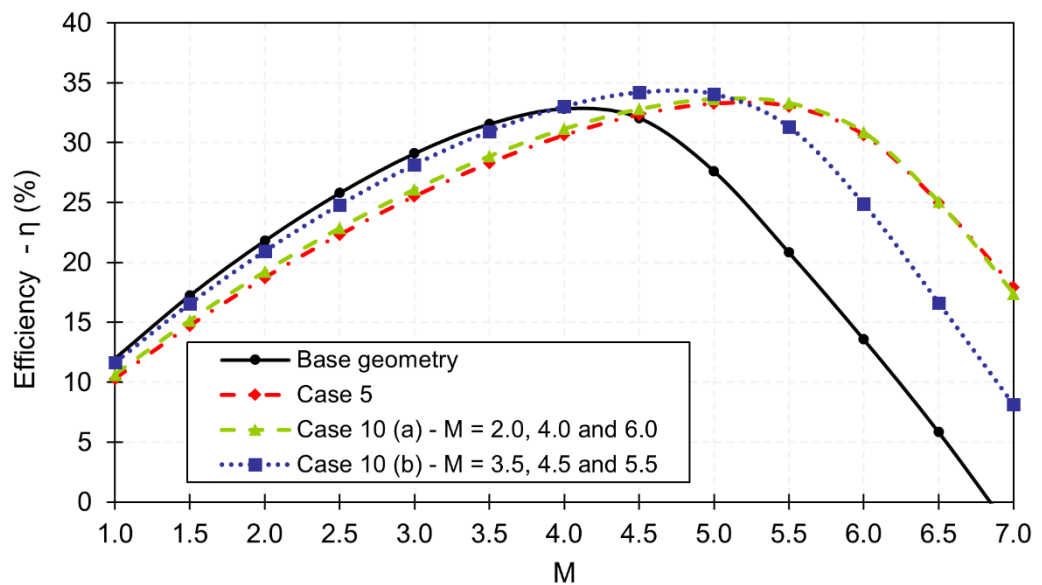
Table 15 - Optimization result for case 10 (a) and (b) using the combined objective function in Eq. (44) which is the sum of the efficiencies for three M values

(a) $M = 2.0, 4.0 \text{ e } 6.0$									
Parameters								Objective function	
p_1	p_2	p_3	p_4	p_5	p_6	p_7	p_8	Initial	Optimized
1.0266	1.1745	1.1945	1.7813	1.093	0.93501	0.6495	-0.02	0.6822	0.8128
(b) $M = 3.5, 4.5 \text{ e } 5.5$									
Parameters								Objective function	
p_1	p_2	p_3	p_4	p_5	p_6	p_7	p_8	Initial	Optimized
0.80832	1.0214	1.0444	1.2081	1.2053	0.89888	0.95914	-0.02	0.8450	0.9661

When comparing the efficiency curves of case 10 (a) and case 5 in Figure 19, it is observed that the differences between them are not very significant. The optimizations for $M = 5.5$, in case 5, and for three values of M , in case 10, had the same effect on the efficiency curve. The lower value of M ($M = 2$) had little influence on the optimization and on the efficiency curve, which showed higher values than the base case for M above 4.5. For case 10 (b), there is a slight shift of the efficiency curve to the left, with efficiency values close to that of the base case for $M < 4$.

Through the efficiency curves of Figure 19, it is possible to notice a predominance of the effect of highest values of M in the optimization, since the increase in the objective function for the optimization of case 10 (a) occurs due to the increase in efficiency in $M = 6$, which is significantly large and capable of canceling the effect of the drop in efficiency for the other two values of M (2 and 4). In case 10 (b), the increase in the objective function is also due to the efficiency gain in the highest M ($M = 5.5$), since the efficiency for $M = 3.5$ decreases and for $M = 4.5$ there is an insignificant increase. It is noteworthy that, for both cases, the weight of each efficiency in the objective function is the same.

Figure 19 - Efficiency curve for cases 5 and 10 (a and b) compared to the base geometry curve



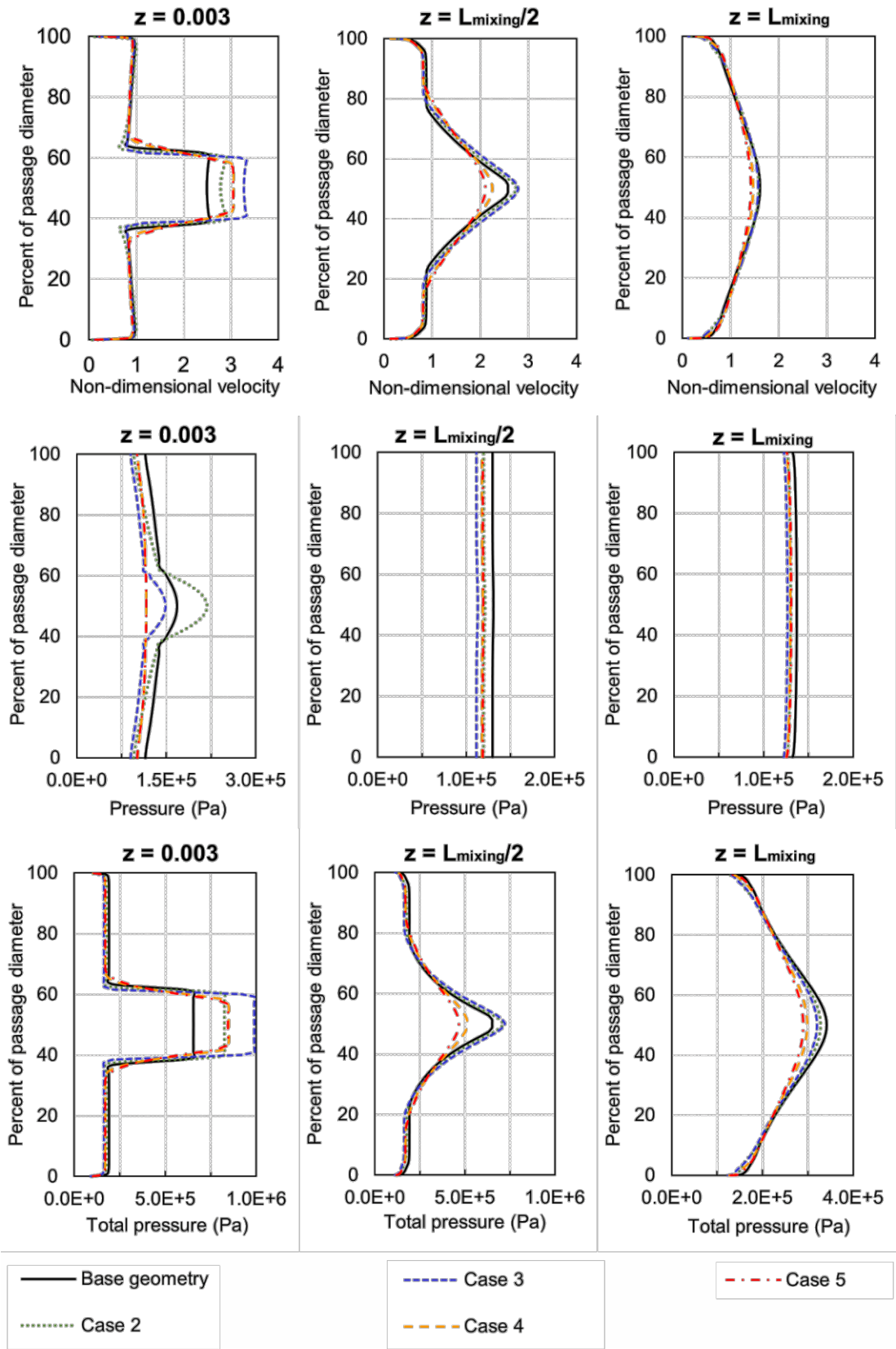
4.6 Influence of geometries on pressure and velocity profiles

Figure 20 shows the velocity, static pressure and total pressure profiles, for base case, case 2, 3, 4 and 5, in three positions along the mixing chamber: inlet ($z =$

0.003 m), middle ($z = L_{mixing}/2$) and outlet ($z = L_{mixing}$). The velocity profile is plotted in terms of the non-dimensional velocity that corresponds to the ratio of the local axial velocity to the average axial velocity calculated based on total discharge and the area of the mixing chamber. A non-dimensional velocity value around 1 indicates that the mixture between the two fluids is nearly completed.

The non-dimensional velocity, static pressure and total pressure profiles show greater homogeneity for cases 4 and 5. These two cases are the ones with the highest efficiency for the entrainment ration values above 4.5, especially for the analyzed entrainment ration ($M = 5.5$). The homogeneity of the profiles indicates a greater mixture between the fluids (non-dimension velocity close to 1) and less dissipation, due to the lower gradients.

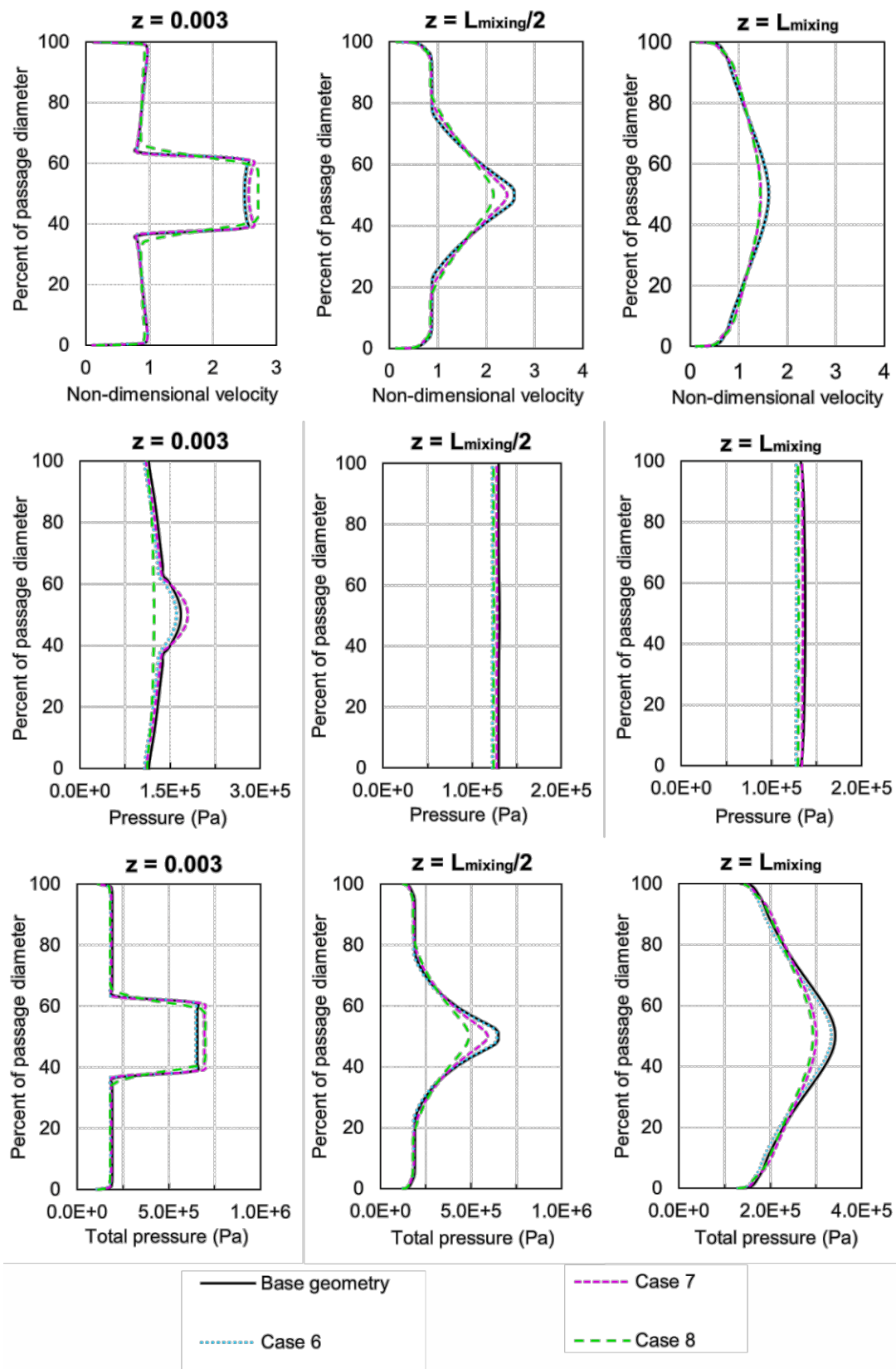
Figure 20 - Velocity, static pressure and total pressures profiles for base geometry and cases 2, 3, 4 and 5 calculated for $M = 5.5$



For cases 6, 7 and 8, the non-dimensional velocity, static pressure and total pressure profiles can be seen in Figure 21. It is also possible to notice the effect of the profiles homogenization for the cases that showed greater efficiency (cases 7 and 8). Although the mixing section of the ejector optimized for case 7 is longer than that of the ejector in case 8, the effect of increasing the NXP in case 8 makes the pressure and velocity profiles very similar at the mixing chamber outlet.

Comparing the efficiency curve and the velocity and pressure profiles for cases 7 and 8, it appears that the effect of increasing the length of the mixing chamber or increasing the NXP is practically the same, in terms of increasing the efficiency of the ejector and mixing behavior of the two fluids.

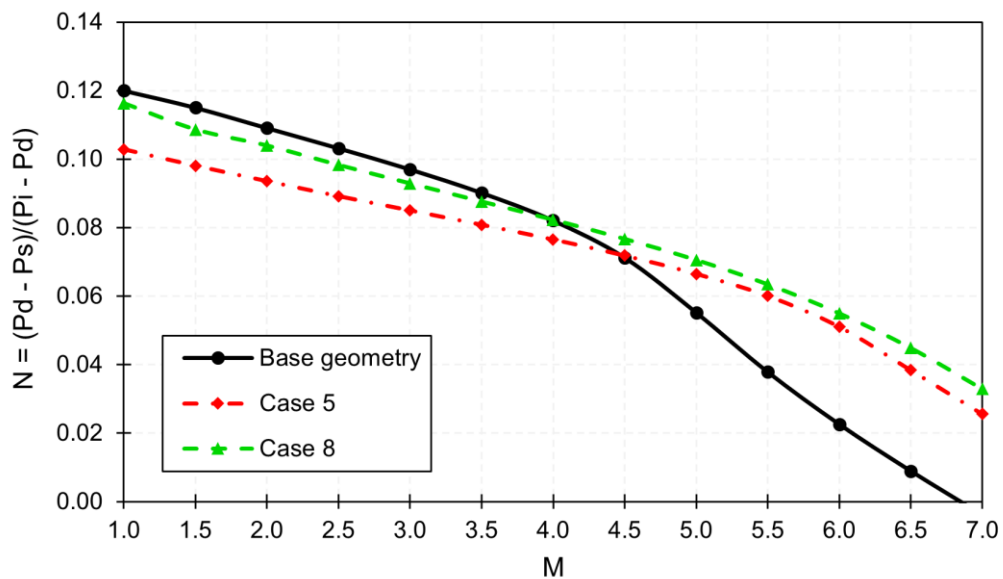
Figure 21 - Velocity, static pressure and total pressures profiles for base geometry and cases 6, 7 and 8 calculated for $M = 5.5$



4.7 Effect of optimizations on pressure ratio

The graph in Figure 22 shows the pressure gain N curves (equation 43) for the most efficient cases: case 5 (which did not consider the diffuser curve in the optimization) and case 8, compared with pressure ratio of the base case. It can be observed that the pressure ratio curve for the base case shows a sharp drop, starting from $M = 4$, which is mainly due to the diffuser not working properly: this is further supported by viewing the energy dissipation rate field. The optimized cases, in turn, are smoother and the decrease in N occurs almost uniformly, according to the value of M increases. The monotonic drop in the pressure ratio with the increase in the entrainment ratio is justified, since the pressure losses are proportional to the square of the flow rate. Considering that the flow ratio of the primary fluid is fixed, higher values of M imply higher flows ratio of the secondary and, therefore, higher total flow rates.

Figure 22 - Pressure ratio as a function of the entrainment ratio for base geometry, case 5 and case 8



4.8 Influence of geometries on energy dissipation rate fields

Figure 23 shows the energy dissipation rate fields, in W/m^3 , for the base case, case with diffuser parameterization (case 6) and optimized cases (case 2 to 5, 7 and 8) for $M = 5.5$. When looking at the base case, it is possible to notice that there is a visible region of high energy dissipation in the diffuser, close to the wall. In this same region, a wider spacing of the flow streamlines in relation to the wall is observed, as shown in Figure 24 (a) in comparison to cases 5 (Figure 24 (b)) and 8 (Figure 24 (c)). In the optimized cases, the energy dissipation rate in this region decreases and the

improved flow field has restricted the dissipation to the mixing chamber. It is observed that the reduction in the region of energy dissipation accompanies the increase in energy efficiency, when comparing the cases 2 to 5. Case 5 presents greater efficiency for $M = 5.5$ compared to base cases, 2, 3 and 4 and energy dissipation field more restricted to the mixing section region. Thus, it is noted that the optimization of the Bézier curves at the fluid inlets, the nozzle and the NXP affect the energy dissipation fields, restricting the regions in which the dissipation occurs.

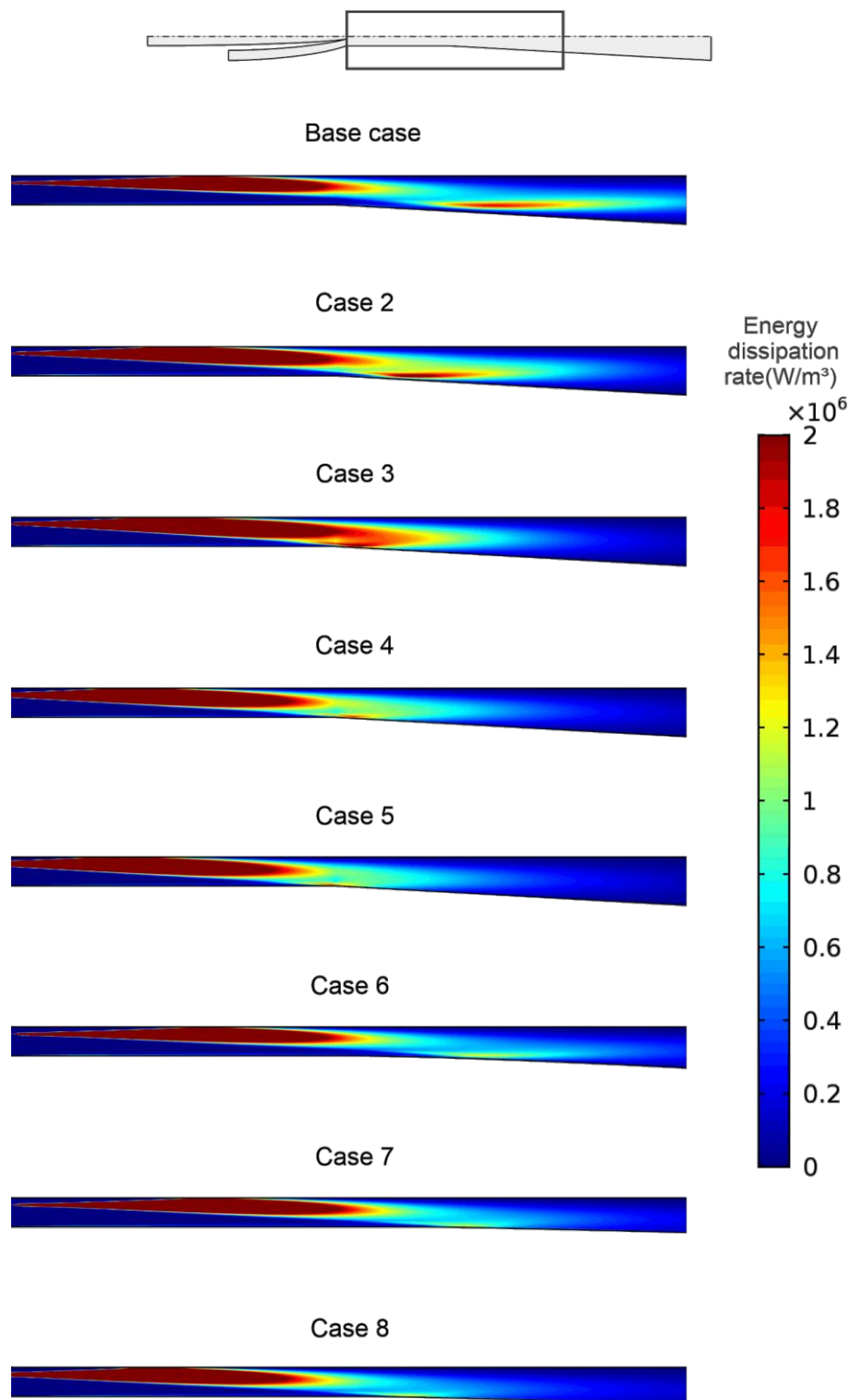
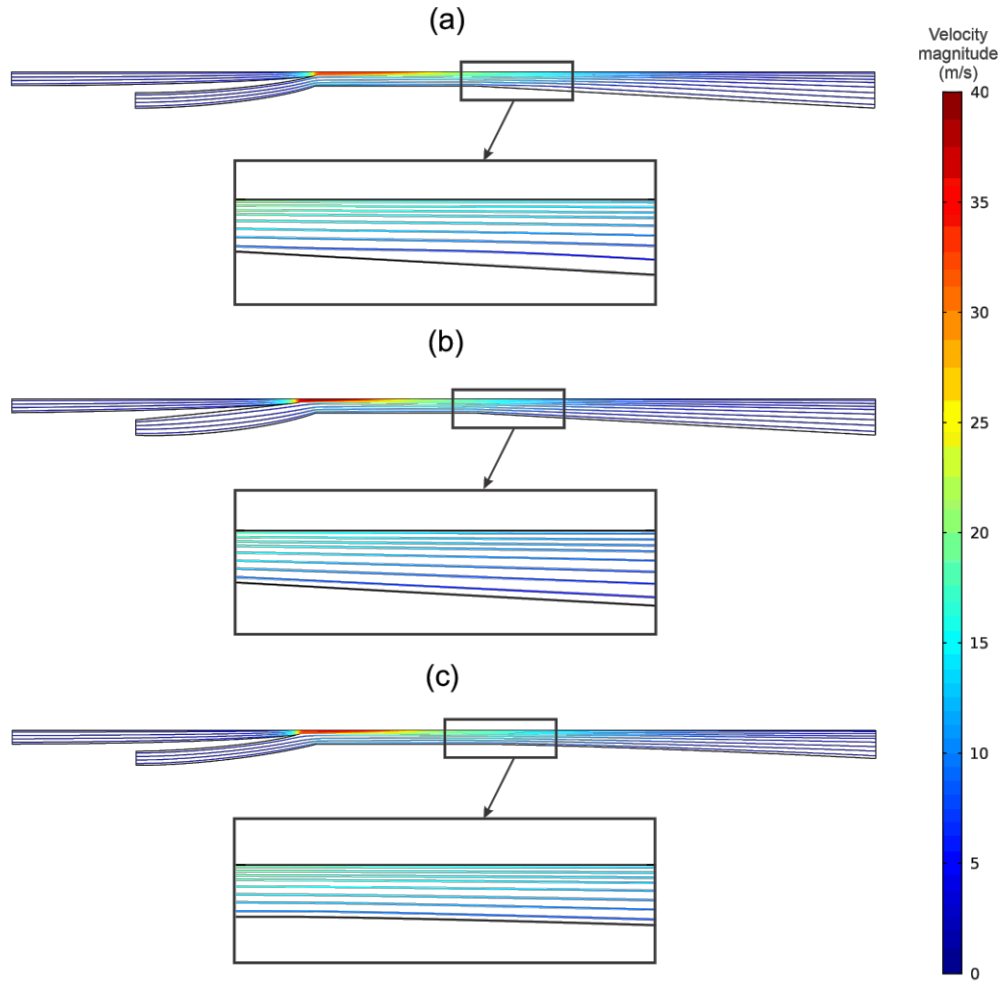
Figure 23 - Energy dissipation fields in the region of the mixing section and diffuser inlet for $M = 5.5$ 

Figure 24 - Streamlines for $M = 5.5$ in base case (a), case 5 (b) and case (8)

Case 6, which presents the diffuser curve parameterized as a quadratic Bézier curve and no optimization performed, also has a dissipation region close to the diffuser wall. However, this dissipation is less than that observed in the base case. As the inlet, nozzle and NXP regions are the same for the base case and case 6, it is observed that the parameterization of the diffuser also influenced the decrease in energy dissipation. With optimization performed in cases 7 and 8, dissipation is more restricted to the mixing chamber, as in the other cases already analyzed.

In general, energy dissipation occurs in the shear layer, a region in which the momentum transfer between the primary and secondary fluid occurs as the working principle of ejectors. This region of concentration of energy dissipation rate can be seen in all cases, on the left side of the images in the Figure 23, which shows the mixing chamber inlet, where the primary and secondary fluids meet.

5 CONCLUSIONS

Numerical simulations were performed to optimize the curves of a water ejector. For optimization, Bézier curves were used because of their easy construction and parametrization and their availability in CAD software. The optimization's objective was to maximize the efficiency of the ejector. This research brought contributions to the study of LJI ejectors, using an algorithm to optimize the whole geometry of the ejector, with multiple parameters, including the shape of the curves and not just isolated geometric parameters allowing to assess which geometric features are more important to the ejector performance.

The results of the optimizations showed that the efficiency of the ejector is very sensitive to the geometry of the fluid inlet regions (primary inlet, nozzle and suction chamber). This was observed by the optimization of the control points of the curves that delimit these regions. Furthermore, the operational conditions (in this case, the entrainment ratio - M) influence the efficiency curve resulting from the optimization. Optimizations for higher M values, 5.5, for example, as in case 2, generate a smoother efficiency curve with a lower sensitivity of variation of efficiency to changes in flow rates.

The inclusion of parameters to optimize the nozzle diameter, NXP, mixing length, diffuser curve and diameter in the simulations resulted in optimized geometries that presented higher efficiency values. The importance of these geometric parameters in the evaluation of the ejector's performance was confirmed by the analysis of cases 4 to 8. In the comparison of cases 5, 7 and 8, it was also observed that when the value of the NXP is greater, the optimized length of the mixing chamber is less than when the NXP was 0. On the other hand, the inclusion of parameters to optimize the diameter of the fluid inlets has not shown significant changes in the efficiency of the ejector.

When analyzing the effect of changes in geometry caused by the optimizations, it is observed that the velocity and pressure profiles in three sections of the mixing chamber tend to be more homogeneous, and consequently less dissipative, for geometries that showed greater efficiency. This is further confirmed by the local energy dissipation rate fields. Another behavior observed in the optimized cases (greater efficiency) is the occurrence of the most complete mixture between the primary and secondary fluids by the end of the mixing chamber – this effect is mainly governed by

nozzle position NXP and mixing chamber length: this combined effect was only observable because of the multiparametric optimization approach. Energy dissipation rate is also affected by optimizations, making it more restricted to the region of the mixing section, where energy dissipation is inevitable due to jet induced flow, on the optimized cases with higher efficiency.

5.1 Suggestions for future research

Based on what was developed in this work, some possible studies are suggested for the continuity of this research:

- Parameterization of the ejectors with Bézier curves of order 3 or higher. The parameterization of higher orders implies a greater number of parameters to be optimized and, consequently, more options of curve shape, which can be favorable for the proposed problem.
- Optimization of LJM ejector (multiphase), which presents several applications, including in CCS systems. The optimization of this type of ejector involves more complex physics, but the observations of geometric parameters made in this work can guide the optimization of ejectors of greater complexity.

6 REFERENCES

- AIDOUN, Z.; OUZZANE, M. The effect of operating conditions on the performance of a supersonic ejector for refrigeration. **International Journal of Refrigeration**, v. 27, n. 8, p. 974–984, 2004.
- ANDERSON JR., J. D. et al. **Computational fluid dynamics**. Third ed. [s.l: s.n.]. v. 82
- BESAGNI, G.; MEREU, R.; INZOLI, F. Ejector refrigeration: A comprehensive review. **Renewable and Sustainable Energy Reviews**, v. 53, p. 373–407, 2016.
- CHIEREGATTI, B. G. **Optimization based on the adjoint method for Adsorbed Natural Gas Storage Systems**. São Paulo: Escola Politécnica of Universidade de São Paulo, 2019.
- COMSOL MULTIPHYSICS. CFD Module User 's Guide. **COMSOL Multiphysics**, 2017.
- COMSOL MULTIPHYSICS. Optimization Module User's Guide. **COMSOL Multiphysics**, 2018.
- CONN, A. R.; SCHEINBERG, K.; VICENTE, L. N. **Introduction to derivative-free optimization**. [s.l: s.n.]. 2009.
- CUAMATZI-MELÉNDEZ, R.; FLORES-CUAMATZI, E. Modelling fluid-structure interaction of water recirculating flow to predict damage and/or failure in a jet-pump assembly of a nuclear boiling water reactor. **Engineering Structures**, v. 206, n. August 2017, p. 110155, 2020.
- CUI, Z.; QIAN, S.; YU, J. Performance assessment of an ejector enhanced dual temperature refrigeration cycle for domestic refrigerator application. **Applied Thermal Engineering**, v. 168, n. December 2019, p. 114826, 2020.
- CUNNINGHAM, G. Gas Compression With tie Liquid Jet Pump. **Journal of Fluids Engineering**, 1974.
- DONG, J. et al. **Experimental investigation of a miniature ejector using water as working fluid**. ASME 2019 6th International Conference on Micro/Nanoscale Heat and Mass Transfer, MNHMT 2019. **Anais...**Dalian, China: 2019

DROZDOV, A. N. et al. **Stand Research and Analysis of Liquid-Gas Jet-Pump's Operation Characteristics for Oil and Gas Production**. SPE Annual Technical Conference and Exhibition. **Anais...**Denver, Colorado: 2011

ESDU. **Ejectors and jet pumps - design and performance for incompressible liquid flow**ESDU-Engineering Sciences Data Unit, , 1986.

FARIN, G. **Curves and Surfaces for Computer Aided Geometric Design**. 3rd. ed. [s.l.] Academic Press Limited, 1992. v. i

HAUKE, G.; HUGHES, T. J. R. A unified approach to the stability of generalized static neural networks with linear fractional uncertainties and delays. **Computer methods in applied mechanics and engineering**, v. 41, n. 5, p. 1275–1284, 1993.

HEDGES, K.; HILL, P. Compressible Flow Ejectors: Part I—Development of a Finite-Difference Flow Model. **Journal of Fluids Engineering**, v. 96, n. 3, p. 272–281, 1974.

HIRSCH, C. **Numerical Computation of Internal and External Flows**. Second ed. ed. [s.l.] Elsevier, 2007. v. 53

IPCC. **IPCC special report on carbon dioxide capture and storage**. New York: Cambridge University Press, 2006.

KULFAN, B. M.; BUSSOLETTI, J. E. “Fundamental” parametric geometry representations for aircraft component shapes. **11th Multidisciplinary Analysis and Optimization Conference**, v. 1, p. 547–591, 2006.

LAWRENCE, N.; ELBEL, S. Experimental Investigation of a Two-Phase Ejector Cycle Suitable for Use with Low- Pressure Refrigerants R134a and R1234yf. **International Journal of Refrigeration**, 2013.

LEE, D.; WISWALL, M. A parallel implementation of the simplex function minimization routine. **Computational Economics**, v. 30, n. 2, p. 171–187, 2007.

LIMA NETO, I. E. Maximum suction lift of water jet pumps. **Journal of Mechanical Science and Technology**, v. 25, n. 2, p. 391–394, 2011.

LIU, F.; LI, D.; ZENG, X. Research on Energy Saving Technology of Distributing Combined Adjustable Jet Pump. **Procedia Engineering**, v. 205, p. 738–743, 2017.

LIU, J. et al. The influence of the area ratio on ejector efficiencies in the MED-TVC

desalination system. **Desalination**, v. 413, p. 168–175, 2017.

LIU, J. et al. Thermodynamic analysis of the steam ejector for desalination applications. **Applied Thermal Engineering**, v. 159, n. April, p. 113883, 2019.

LIU, X.; ZHAN, Q.; LIA, Y. The application analysis of jet pump in heating system. **Procedia Engineering**, v. 205, p. 2208–2214, 2017.

LIU, Y.; TU, Z.; CHAN, S. H. Applications of ejectors in proton exchange membrane fuel cells: A review. **Fuel Processing Technology**, v. 214, n. November 2020, p. 106683, 2021.

LUCAS, C.; KOEHLER, J. Experimental investigation of the COP improvement of a refrigeration cycle by use of an ejector. **International Journal of Refrigeration**, v. 35, n. 6, p. 1595–1603, 2012.

MALLELA, R.; CHATTERJEE, D. Numerical investigation of the effect of geometry on the performance of a jet pump. **Proceedings of the Institution of Mechanical Engineers, Part C: Journal of Mechanical Engineering Science**, v. 225, n. 7, p. 1614–1625, 2011.

MANGIALARDO, A. et al. Numerical investigation on a jet pump evolving liquid lead for GEN-IV reactors. **Nuclear Engineering and Design**, v. 280, p. 608–618, 2014.

MARUM, V. J. DE O. et al. Performance analysis of a water ejector using Computational Fluid Dynamics (CFD) simulations and mathematical modeling. **Energy**, v. 220, p. 119779, 2021.

MENTER, F. R. Zonal two-equation k - ω turbulence model for aerodynamic flows. **AIAA Journal**, 1993.

MENTER, F. R. Two-equation eddy-viscosity turbulence models for engineering applications. **AIAA Journal**, v. 32, n. 8, p. 1598–1605, 1994.

MENTER, F. R.; KUNTZ, M.; LANGTRY, R. Ten Years of Industrial Experience with the SST Turbulence Model. **Turbulence, Heat and Mass Transfer 4**, v. 576, p. 60–63, 2003.

NELDER, J. A.; MEAD, R. A simplex method for function minimization. **The Computer Journal**, v. 7, n. 4, p. 308–313, 1965.

PALACZ, M. et al. CFD-based shape optimisation of a CO₂ two-phase ejector mixing section. **Applied Thermal Engineering**, v. 95, p. 62–69, 2016.

PEDROSO, M. C. **Dinâmica dos fluidos computacional aplicada a ejetores**. [s.l.] Universidade Estadual de Campinas, 2015.

PRAUTZSCH, H.; BOEHM, W.; PALUSZNY, M. **Bezier and B-Spline Techniques**. 1st. ed. [s.l.] Springer, 2002.

RAZA, A. et al. Significant aspects of carbon capture and storage – A review. **Petroleum**, v. 5, n. 4, p. 335–340, 2019.

REDDICK, C.; SORIN, M.; RHEAULT, F. Energy savings in CO₂ (carbon dioxide) capture using ejectors for waste heat upgrading. **Energy**, v. 65, p. 200–208, 2014.

RIFFAT, S. B.; GAN, G.; SMITH, S. Computational fluid dynamics applied to ejector heat pumps. **Applied Thermal Engineering**, v. 16, p. 291–297, 1996.

SANGER, N. L. Noncavitating and cavitating performance of two low-area-ratio water jet pumps with throat lengths of 5.66 diameters. **Nasa Technical Note**, 1968a.

SANGER, N. L. Cavitating performance of two low-area-ratio water jet pumps having throat lengths of 7.25 diameters. **NASA Technical Note**, 1968b.

SANGER, N. L. An Experimental Investigation of Several. **Journal of Basic Engineering**, p. 11–19, 1970.

SARSHAR, S. The recent applications of jet pump technology to enhance production from tight oil and gas fields. **Society of Petroleum Engineers - SPE Middle East Unconventional Gas Conference and Exhibition 2012, UGAS - Unlocking Unconventional Gas: New Energy in the Middle East**, p. 296–314, 2012.

SIMONI, R. **Teoria Local das Curvas**. [s.l.] Universidade Federal de Santa Catarina, 2005.

SU, L.; AGARWAL, R. K. CFD simulation of a supersonic steam ejector for refrigeration application. **American Society of Mechanical Engineers, Fluids Engineering Division (Publication) FEDSM**, p. 1–4, 2015.

TASHTOUSH, B. M.; AL-NIMR, M. A.; KHASAWNEH, M. A. A comprehensive review of ejector design, performance, and applications. **Applied Energy**, v. 240, n. February,

p. 138–172, 2019.

VARGA, S. et al. Experimental and numerical analysis of a variable area ratio steam ejector. **International Journal of Refrigeration**, v. 34, n. 7, p. 1668–1675, 2011.

VARGA, S.; OLIVEIRA, A. C.; DIACONU, B. Influence of geometrical factors on steam ejector performance - A numerical assessment. **International Journal of Refrigeration**, v. 32, n. 7, p. 1694–1701, 2009.

VERSTEEG, H. K.; MALALASEKERA, W. **An Introduction to Computational Fluid Dynamics**. Second ed. [s.l.] Pearson, 2007. v. 2

VUTUKURU, R.; PEGALLAPATI, A. S.; MADDALI, R. Thermodynamic studies on a solar assisted transcritical CO₂ based tri-generation system with an ejector for dairy applications. **International Journal of Refrigeration**, v. 108, p. 113–123, 2019.

WANG, H.; WANG, H. Enhance hydraulic balance of a district cooling system with multiple jet pump. **Energy Procedia**, v. 158, p. 2536–2542, 2019.

WINOTO, S. H.; LI, H.; SHAH, D. A. Efficiency of Jet Pumps. **Journal of Hydraulic Engineering**, n. February, p. 150–156, 2000.

XU, M. et al. Experimental investigation on the transport of different fish species in a jet fish pump. **Aquacultural Engineering**, v. 79, n. August, p. 42–48, 2017.

XU, M. et al. Impact of fish locomotion on the internal flow in a jet fish pump. **Ocean Engineering**, v. 187, n. July, p. 106227, 2019.

XU, M. et al. Impact of pressure gradients on fish scales in a jet fish pump. **Biosystems Engineering**, v. 191, p. 27–34, 2020.

YADAV, R. L.; PATWARDHAN, A. W. Design aspects of ejectors: Effects of suction chamber geometry. **Chemical Engineering Science**, v. 63, n. 15, p. 3886–3897, 2008.

YAN, J.; LI, S.; LIU, Z. Numerical investigation on optimization of ejector primary nozzle geometries with fixed/varied nozzle exit position. **Applied Thermal Engineering**, v. 175, n. May, p. 115426, 2020.

YAN, T. et al. Study on energy conservation water injection system of offshore platform based on jet pump. **Journal of Petroleum Science and Engineering**, v. 170, n. June,

p. 368–373, 2018.

YAPICI, R.; ALDAŞ, K. Optimization of water jet pumps using numerical simulation. **Proceedings of the Institution of Mechanical Engineers, Part A: Journal of Power and Energy**, v. 227, n. 4, p. 438–449, 2013.

ZHU, Y. et al. Numerical investigation of geometry parameters for design of high performance ejectors. **Applied Thermal Engineering**, v. 29, n. 5–6, p. 898–905, 2009.